–Title of my thesis–

Shreeprasad Bhat

A Thesis Submitted to

Indian Institute of Technology Hyderabad

In Partial Fulfillment of the Requirements for

The Degree of Master of Technology

Department of Artificial Intelligence

June 2022

Declaration

I declare that this written submission represents my ideas in my own words, and where ideas or words of others have been included, I have adequately cited and referenced the original sources. I also declare that I have adhered to all principles of academic honesty and integrity and have not misrepresented or fabricated or falsified any idea/data/fact/source in my submission. I understand that any violation of the above will be a cause for disciplinary action by the Institute and can also evoke penal action from the sources that have thus not been properly cited, or from whom proper permission has not been taken when needed.

_____

(Signature)

_____

(Shreeprasad Bhat)

_____

(Roll No.)

Approval Sheet

This Thesis entitled –Title of my thesis– by Shreeprasad Bhat is approved for the degree of Master of Technology from IIT Hyderabad

---

(———-) Examiner
Dept. of Chem Eng
IITH

(———-) Examiner
Dept. Math
IITH

(Dr. Shantanu Desai) Adviser
Dept. of Physics
IITH

(———) Chairman
Dept. of Artificial Intelligence
IITH

Dedication

Abstract

Contents

Chapter 1

Model-independent distance calibration of Gamma-Ray Bursts

1.1 Introduction

The accelerating expansion of the universe is first found from the fact that the luminosity of type Ia supernovae (SNe Ia) is dimmer than expected [1]. This led to the discovery of Dark energy [2]. The default expectation is the simplest model for the Dark Energy, where it does not change in time. This can be parametrized with the equation of state of the Dark Energy. The concordance case has w = -1 at all times, and this is the expectation of Einstein's cosmological constant, or if the Dark Energy arises from vacuum energy. Given the strong results from supernovae for redshifts of less than 1, the frontier has now been pushed to asking the question of whether the value of w changes with time (and redshift).

The best way to measure properties of the Dark Energy seems to be to measure the expansion history of our Universe and place significant constraints on models of the Universe. Hubble diagram can be used to measure it. The Hubble diagram (HD) is a plot of distance versus redshift, with the slope giving the expansion history of our Universe. been proposed to determine the distances and redshifts of two thousand supernovae per year out to redshift 1.7 with exquisite accuracy. The default expectation is the simplest model for the Dark Energy, where it does not change in time. This can be parameterized with the equation of state of the Dark Energy. The best way to measure whether dark energy changed with respect to redshift, is to measure it over wide range of redshifts, but supernovaes cannot be deteceted above 1.7 even with modern satelites. But GRBs offer means extend HD over redshift > 6. The reason is that GRBs are visible across much larger distances than supernovae.

GRBs are now known to have several light curve and spectral properties from which the luminosity of the burst can be calculated (once calibrated), and these make GRBs into 'standard candles'. Several interesting correlations among Gamma Ray Burst (GRB) observables with available redshifts have been recently identified. Proper evaluation and calibration of these correlations may facilitate the use of GRBs as standard candles constraining the expansion history of the universe up to redshifts of $z > 6$.

1.2 Literature Survey

A remarkable progress in the observation of gamma-ray bursts (GRBs) has been the identification of several very good correlations among the GRB observables ($\tau_{lag} - L, V - L, E_{peak} - L, E_{peak} - E_{gamma}, \tau_{RT} - L, E_{peak} - E_{\gamma,iso}$)[3]. Since then GRBs are proposed to use standard candles. But, all the GRB correlations have been obtained by fitting a hybrid GRB sample without discriminating the redshift. Then, inevitably, the effect of the GRB evolution with the redshift, and the selection effects, have been ignored. [4] shows that not all luminosity correlations are applicable across all redshifts, particularly they show correlation parameters for $E_{iso} - E_{\gamma}$ varies significantly across redshifts. However, [5] finds no statistically significant evidence for redshift dependence of correlation parameters. They also find that one of the five correlation relations tested ($E_{peak} - E_{\gamma}$) has a significantly lower intrinsic dispersion compared to the other correlations. [6] calculates luminosity correlations for updated GRB data and found that finds no statistically significant evidence for redshift dependence of correlation parameters. They also find find that the intrinsic scatter of the $V - L$ correlation is too large and there seems no inherent correlation between the two parameters using the latest GRB data. However all the above assumed a flat universe model to test the luminosity dependence. [7] have proposed a model independet method to test luminosity correlations of Gamma Ray Bursts, and found that there is no evidence for redshift dependence for $E_{peak} - E_{gamma}$ relation.

In this work, we have explored both two popular non-parametric regression techniques Gaussian Process and Deep Learning for reconstruction of redshift-distance modulus. The rest of sections are organized as follows. 1.3 descirbes the dataset. 1.4 descirbes the machine learning techniques and architectures used. 1.5 discusses the results from Gaussian processes using Pantheon sample. 1.6 discusses results from Deep Learning using Pantheon sample. 1.7 results of GP and Deep Learning from Union2.1 sample. 1.8 mentions the conclusion.

1.3 Observational Data

1.3.1 GRB

The GRB dataset we use is from [6]. In Table 1, we list the variables of 116 GRBs that we use in fitting luminosity correlations

1.3.2 Pantheon

Pantheon compilation [8] is the combined sample of SNe Ia discovered from different surveys to form the largest sample consisting of total of 1048 SNe Ia raning from $0.01 < z < 2.3$.

1.3.3 Union

The updated supernova Union2.1[9] compilation of 580 SNe is available at [1]

[1] http://supernova.lbl.gov/Union

1.4 Methodology

1.4.1 Gaussian Processes

Gaussian Processes is a non-parametric regression technqiue, in the sense that we don't make any assumption about the function form. We define a prior probability distribution over functions y(x), such that set of values evaluated at $x_1, x_2...x_n$ follow gaussian distribution. This joint gaussian distributino is specified by mean and covariance. In most applications, we will not have any prior knowledge about the mean of y(x) and so by symmetry we take it to be zero. The covariance of y(x) evaluated at any two values of x, which is given by the kernel function $k(x, x')$. A Gaussian Process is completely specified by its mean function and covariance function. We define mean function $m(x)$ and the covariance function $k(x, x')$ of real process $f(x)$ as

$$m(\mathbf{x}) = \mathbb{E}\left[f(\mathbf{x})\right] \tag{1.1}$$

$$k(\mathbf{x}, \mathbf{x'}) = \mathbb{E}\left[(f(\mathbf{x}) - m(\mathbf{x}))(f(\mathbf{x'}) - m(\mathbf{x'}))\right] \tag{1.2}$$

and will write the Gaussian process as

$$f(\mathbf{x}) \approx GP\left(m(\mathbf{x}), k(\mathbf{x}, \mathbf{x'})\right) \tag{1.3}$$

We will assume mean function of prior to be zero, since it's difficult predict the mean.

$$\begin{bmatrix} \mathbf{f} \\ \mathbf{f}_* \end{bmatrix} = \mathcal{N}\left(\mathbf{0}, \begin{bmatrix} K(\mathbf{X}, \mathbf{X}) & K(\mathbf{X}, \mathbf{X}_*) \\ K(\mathbf{X}_*, \mathbf{X}) & K(\mathbf{X}_*, \mathbf{X}_*) \end{bmatrix}\right)$$

If there are $\mathbf{n}$ training points and $\mathbf{n}_*$ test points then $K(\mathbf{X}, \mathbf{X'})$ denotes the $\mathbf{n} \times \mathbf{n^*}$ matrix of the covariances evaluated at all pairs of training and test points, and similarly for the other entries $K(\mathbf{X}, \mathbf{X}_*)$, $K(\mathbf{X}_*, \mathbf{X}_*)$ and $K(\mathbf{X}_*, \mathbf{X}_*)$. To get the posterior distribution over functions we need to restrict this joint prior distribution to contain only those functions which agree with the observed data points. In probabilistic terms this operation is extremely simple, corresponding to conditioning the joint Gaussian prior distribution on the observation to give

$$\mathbf{f}_*|X_*, X.\mathbf{f} \quad \approx \quad \mathcal{N}\left(K(X_*, X)K(X, X)^{-1}\mathbf{f}, K(X_*, X_*) - K(X_*, X)K(X, X)^{-1}K(X, C_*)\right)$$

Function values $\mathbf{f}_*$ (corresponding to test inputs X_*) can be sampled from the joint posterior distribution by evaluating the mean and covariance matrix from (**??**) and generating samples. The marginal likelihood(or evidence) $p(y|X)$. The marginal likelihood is the integral of the likelihood times the prior

$$p(\mathbf{y}|X) = \int p(\mathbf{y}|\mathbf{f}, X)p(\mathbf{f}|X)d\mathbf{f} \tag{1.4}$$

The term marginal likelihood refers to the marginalization over the function values $\mathbf{f}$. Under the Gaussian process model the prior is Gaussian, $\mathbf{f}|X \approx \mathcal{N}(\mathbf{0}, K)$ or

$$\log p(\mathbf{f}|\mathbf{X}) = -\frac{1}{2}\mathbf{f}^T K^{-1}\mathbf{f} - \frac{1}{2}log|K| - \frac{n}{2}log2\pi \tag{1.5}$$

and the likelihood is a factorized Gaussian $\mathbf{y}|\mathbf{f} \approx \mathcal{N}(\mathbf{f}, \sigma_n^2 I)| - \frac{n}{2}log2\pi$ This result can also be obtained

directly by observing that $\mathbf{y} \approx \mathcal{N}(\mathbf{0}, K + \sigma_n^2 I)$.

A practical implementation of Gaussian process regression is proposed in [10]. The algorithm uses Cholesky decomposition, instead of directly inverting the matrix, since it is faster and numerically more stable. The algorithm returns the predictive mean and variance for noise free test data to compute the predictive distribution for noisy test data $\mathbf{y}_*$, simply add the noise variance σ_n^2 to the predictive variance of f_*.

1.4.2 Recurrent Neural Networks

Recently, the application of deep learning in cosmological research is very extensive and successful. Following the work of [11], we reconstruct the distance moduli from the Pantheon compilation [8] with RNN+BNN. In this process, the reconstruction of distance only depends on the dataset, and without any assumption on the cosmological model.

RNN is a class of nets which can predict the future from the complex sequential information without any model assumption, but is incapable of estimating the uncertainty of target. This shortcoming can be fixed up with BNN. Therefore, our neural network is composed of RNN and BNN, the details of which are described bellow.

Handling long sequences, the training of RNN will take a long time and the information of initial inputs will gradually fades away. Thus, we adopt the time step $t = 4$ to alleviate the long training time, and use the most popular basic cell called Long Short-Term Memory (LSTM) cell to solve the problem of information loss. RNN with LSTM cell is aware of what to store, throw away and read. The architecture of LSTM is shown in Figure (1.1). In the unrolled RNN, the neurons at each time step t receive the inputs as well as the outputs from the previous time step. In the neural network, the loss function is used to depict the difference between the targets and the predicts. We adopt the Mean Squared Error (MSE) function as the loss function and find the minimum with the Adam optimizer.

LSTM Cell

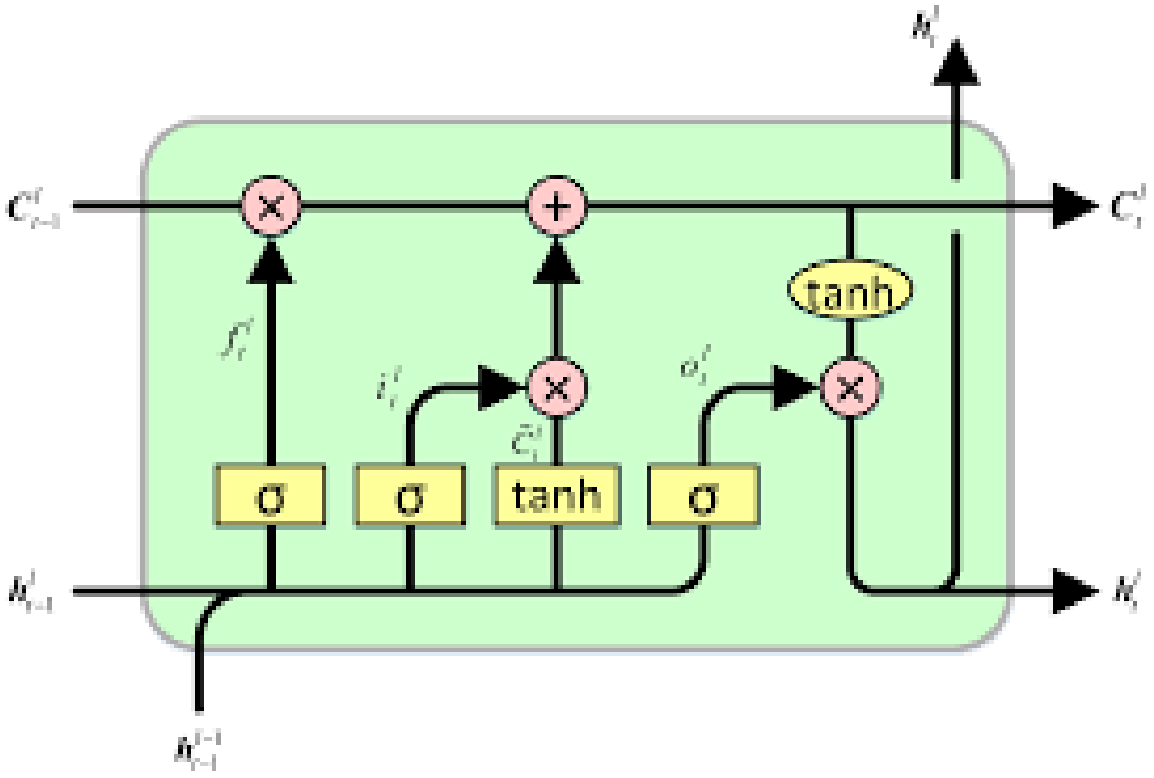

Figure 1.1: Neural Network Architecture

The computations of LSTM are

$$i^{<t>} = \sigma\left(W_{xi}^T \cdot x^{<t>} + W_{hi}^T \cdot h^{<t-1>} + b_i\right) \tag{1.6}$$

$$f^{<t>} = \sigma\left(W_{xf}^T \cdot x^{<t>} + W_{hf}^T \cdot h^{<t-1>} + b_f\right) \tag{1.7}$$

$$o^{<t>} = \sigma\left(W_{xo}^T \cdot x^{<t>} + W_{ho}^T \cdot h^{<t-1>} + b_o\right) \tag{1.8}$$

$$g^{<t>} = A_f\left(W_{xg}^T \cdot x^{<t>} + W_{hg}^T \cdot h^{<t-1>} + b_g\right) \tag{1.9}$$

$$c^{<t>} = f < t > \otimes c^{<t-1>} + i^{<t>} \otimes g^{<t>}, \tag{1.10}$$

$$y^{<t>} = h^{<t>} = o^{<t>} \otimes A_f\left(c^{<t>}\right), \tag{1.11}$$

where σ is the sigmoid function that outputs a value between 0 and 1, t is the time step referring to the current sequence (for example $t = 1$ for the first redshift). The superscript $< t >$ indicates a vector of steps t, the superscript T is the transpose of the matrix, the dot is matrix product and $\otimes$ is direct product. $x^{<t>}$ and $y^{<t>}$ are respectively the current input and output vectors. $h < t >$ and $c^{<t>}$ are respectively the short-term state and long-term state of LSTM cells. A_f is an activation function to make the network be capable of solving complex tasks by introducing the non-linearity to network. In our work, we use the tanh activation function, which is defined as

$$A_{f_{\text{Tanh}}} = \tanh(x) = \frac{e^x - e^{-x}}{e^x + e^{-x}}.$$

Network Architecture

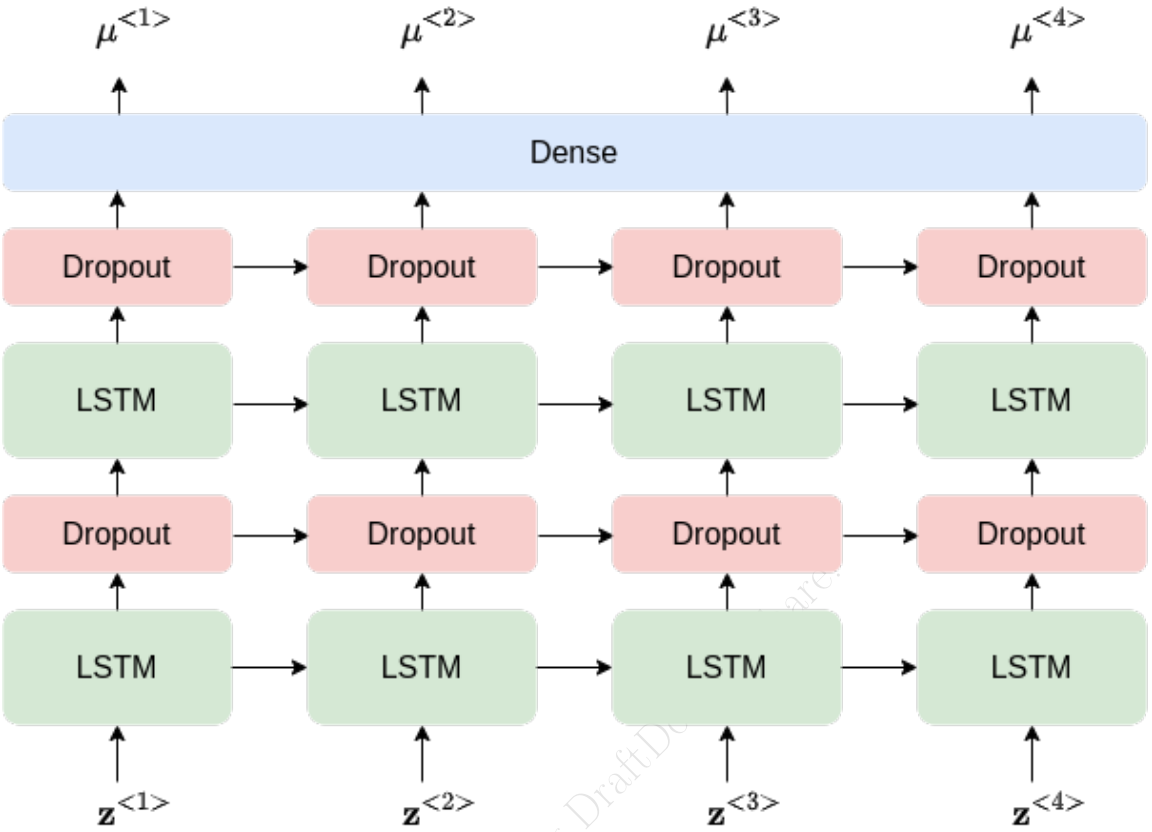

Figure 1.2: Neural Network Architecture

The architecture of our network (1.2), with one hidden layer (left), unrolled through time step $t = 4$ (right). In the unrolled network, each column is one of the t time steps, while the three rows from bottom to top represent input layer, hidden layer and output layer, respectively. The first two layers with tanh activation function consist of LSTM cell containing 100 neurons, while the output layer is a fully-connected (dense) layer. To avoid overfitting, the dropout[12] technique is employed between LSTM and its next layers, and we set the dropout rate to 0.2.

There are four connected layers playing different roles, where the main layer that outputs $g^{<t>}$ analyzes the current inputs $x^{<t>}$ and the previous state $h^{<t-1>}$, the rest three layers are gate controllers: (a) Input gate controlled by $i^{<t>}$ determines which parts of $g^{<t>}$ should be added to $c^{<t>}$, (b) Forget gate controlled by $f^{<t>}$ determines which parts of $c^{<t>}$ should be abandoned, (c) Output gate controlled by $o< t >$ determines which parts of $c^{<t>}$ should be output. It can be easily found that, these gate controllers are related to the logistic activation function σ, thus they would close the gate if output 0 and open it if output 1.W_{xi}, W_{xf}, W_{xo} and W_{xg} are the weight matrices of each of above four layers connecting to the input vector. W_{hi}, W_{hf}, W_{ho}, and W_{hg} are the weight matrices of each of layers connecting to the previous short-term state. b_i, b_f, b_o, and b_g are the bias terms for each of layer.

In a deep neural network, the training may suffer from overfitting due to a large number of its

own hyperparameters. We can use the method called regularization to prevent it from overfitting. Dropout is one of the most popular regularization techniques, applying in some layers to reduce the overfitting risk. In this way, some neurons has a probability of being ignored at every step controlled by dropout rate. Besides, it is also of benefit to estimate the confidence of the training in BNN.

Bayesian Neural Networks

BNN is a supplementary of RNN for calculating the uncertainty of the prediction. BNN is defined in terms of a prior distribution with parameters over the wights $p(\omega)$, which manifests a prior belief about parameters generating the observations. With a given dataset $\{\mathbf{X}, \mathbf{Y}\}$, we can achieve the posterior distribution of the parameters space $p(\omega \mid \mathbf{X}, \mathbf{Y})$. Thus the output of a new input point x can be anticipated by the integration

$$p\left(y^* \mid x^*, \mathbf{X}, \mathbf{Y}\right) = \int p\left(y^* \mid x^*, \omega\right) p(\omega \mid \mathbf{X}, \mathbf{Y}) \mathrm{d}\omega$$

A full BNN is extremely complex. However, [13] developed a new framework casting dropout training in deep neural network as approximate Bayesian inference in deep Gaussian processes and successfully applied in RNN. Their results offer a Bayesian interpretation of the dropout technique, and verify that a network with a dropout is mathematically equivalent to the Bayesian model. When the RNN is well-trained and executed n times, the network is equivalent to BNN. Therefore, we employ the dropout in the training and call the trained network n times to estimate the uncertainty of outputs, where the dropout is an approximation of the Gaussian processes and cooperates with the activation function to determine the confidence regions of prediction.

1.5 Reconstruction and calibration of distance modulus using Gaussian Processes

We first use Gaussian processes to reconstruct $\mu - z$ relation from pantheon data. Gaussian processes can construct function without involving any model assumption. The Gaussian processes only depend on the covariance function $k(x, x')$, which characterizes the correlation between the function value at x to that at x'. There are many covariance functions available, but any covariance function should be positive definite and monotonously decreasing with the increment of distance between x and x'. Here we use the following kernel

$$\mathrm{k(x,\ x')} = \mathrm{ConstantKernel()} + 1.0 * \mathrm{DotProduct(1)} ** 0.1 \tag{1.12}$$

Our kernel (1.12) is a sum of linear, constant kernels. Linear Kernel with exponent is used to capture relation in the data, constant kernel is used as scale magnitude.

1.5.1 Training

We optimize the hyper-parameters of kernels by maximizing the marginal likelihood marginalized over function values f at the whole locations X. We use the publicly available python package sklearn[14] to reconstruct distance modulus as a function of redshift. The results are plotted in

(1.4). The posterior samples drawn from kernel is shown in (1.13b) .In the range where data points are sparse, the uncertainty of the reconstructed function is large. While training GP numerical issues are common to occur, hence we set $\alpha = 0.3$ and standardize the distance modulus before training. We also restart optimizer 100 times, parameters sampled log-uniform randomly from the space of allowed range.

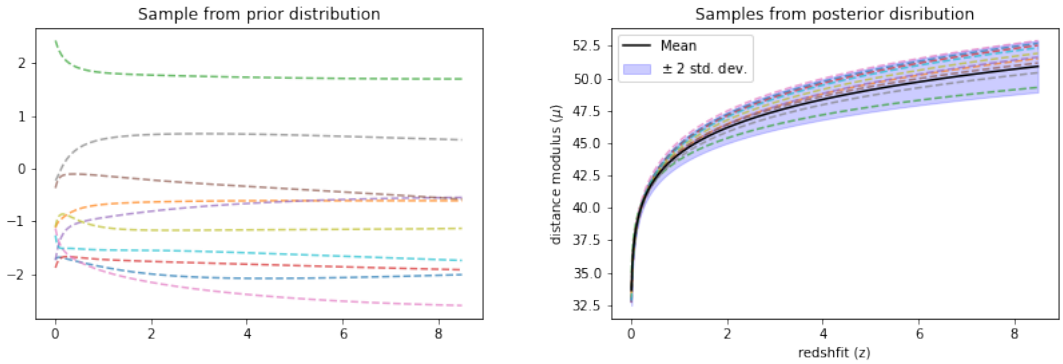

(a) Prior samples drawn from GP

(b) Posterior samples drawn from GP

Figure 1.3: Prior and Posterior distrution samples

The error bars with predictions are shown below

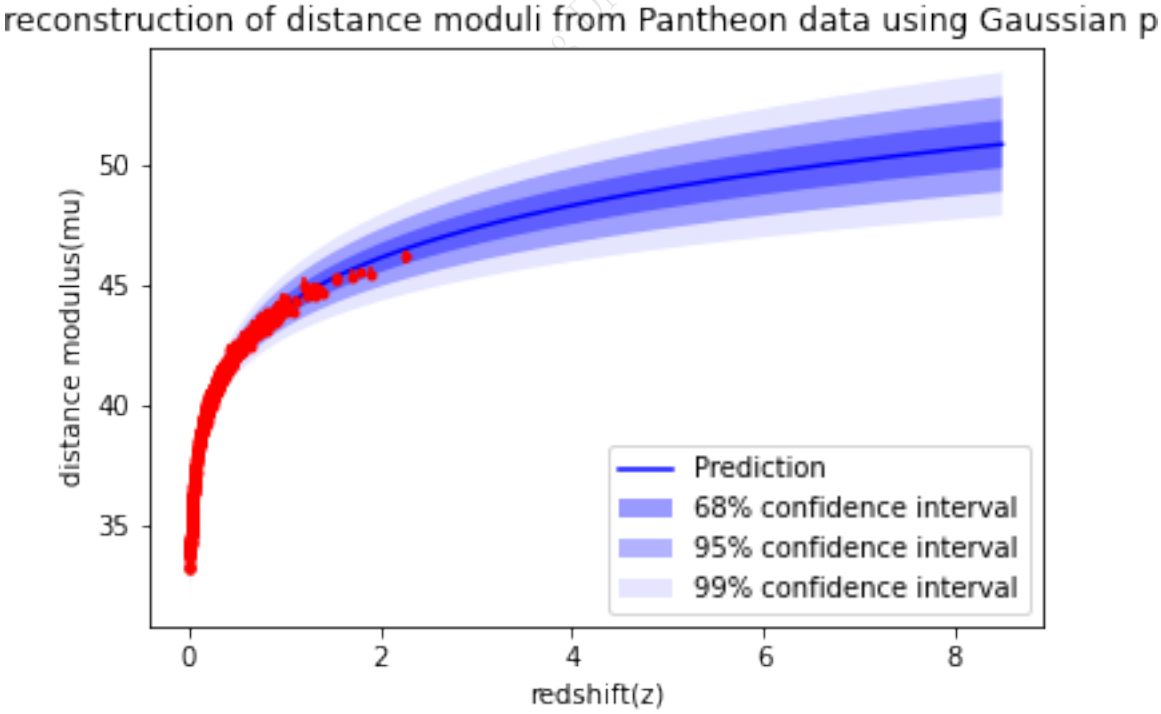

Figure 1.4: The reconstruction of distance moduli from Pantheon data set using GP. The red dots with 1σ error bars are the Pantheon data points. The light-blue dots are the central values of reconstruction. The shaded regions are the 1σ, 2σ and 3σ uncertainties.

Log Marginal Likelihood = -20.3

The coefficient of determination $R^2 = 0.9951$

1.5.2 Testing redshift dependence of luminosity correlations

After reconstructing the redshift-distance modulus from the machine learning model, we can use it fit luminosity correlations. Luminosity correlations are connections between measurable parameters of the GRB vairables(light curves, spectra etc) with the GRB luminosity(L). The burst's luminosity distance must be known to convert P_{bolo} to L (or S_{bolo} to E_γ) and this is known only for bursts with measured redshifts.

$$\mu = 5 \log \frac{d_L}{\text{Mpc}} + 25 \tag{1.13}$$

$$L = 4\pi d_L^2 P_{\text{bolo}} \tag{1.14}$$

We are using the six luminosity correlations defined in [3].

1. Lag versus Luminosity ($T_{lag} - L$)
2. Variability versus Luminosity ($V - L$)
3. E_{peak} versus Luminosity ($E_{peak} - L$)
4. E_{peak} versus E_γ ($E_{peak} - E_\gamma$)
5. T_{RT} versus Luminosity ($T_{RT} - L$)
6. E_{peak} versus E_{iso} ($E_{peak} - E_{iso}$)

The observed luminosity indicators will have different values from those that would be observed in the rest frame of the GRB. That is, the light curves and spectra seen by Earth-orbiting satellites suffer time-dilation and redshift. The physical connection between the indicators and the luminosity is in the GRB rest frame, so we must take our observed indicators and correct them to the rest frame of the GRB.

$$T_{lag_i} = \frac{T_{lag}}{1+z} \tag{1.15}$$

$$T_{RT_i} = \frac{T_{RT}}{1+z} \tag{1.16}$$

$$V_i = V(1+z) \tag{1.17}$$

$$E_{peak_i} = E_{peak}(1+z) \tag{1.18}$$

The calibration will essentially be a fit on a log-log plot of the luminosity indicator versus the luminosity. However, an important point is that the conversion from the observed redshift to a

luminosity distance is independent of any cosmological model.

$$\log \frac{L}{\mathrm{erg\,s^{-1}}} = a_1 + b_1 \log \frac{\tau_{\mathrm{lag},i}}{0.1s}, \tag{1.19}$$

$$\log \frac{L}{\mathrm{erg\ s^{-1}}} = a_2 + b_2 \log \frac{V_i}{0.02}, \tag{1.20}$$

$$\log \frac{L}{\mathrm{erg\ s^{-1}}} = a_3 + b_3 \log \frac{E_{p,i}}{300\mathrm{keV}} \tag{1.21}$$

$$\log \frac{E_\gamma}{\mathrm{erg}} = a_4 + b_4 \log \frac{E_{p,i}}{300\mathrm{keV}}, \tag{1.22}$$

$$\log \frac{L}{\mathrm{erg\ s}} = a_5 + b_5 \log \frac{\tau_{\mathrm{RT},i}}{0.1\ \mathrm{s}}, \tag{1.23}$$

$$\log \frac{E_{\mathrm{iso}}}{\mathrm{erg}} = a_6 + b_6 \log \frac{E_{p,i}}{300\mathrm{keV}} \tag{1.24}$$

Hence, the uncertainty of L propagates from the uncertainties of P_{bolo} and d_L. The isotropic equivalent energy E_{iso} can be obtained from the bolometric fluence S_{bolo} by

$$E_{\mathrm{iso}} = 4\pi d_L^2 S_{\mathrm{bolo}} (1+z)^{-1},$$

the uncertainty of E_{iso} propagates from the uncertainties of S_{bolo} and d_L. If on the other hand, GRBs radiate in two symmetric beams, then we can define the collimation-corrected energy E_γ as

$$E_\gamma \equiv E_{\mathrm{iso}}\, F_{\mathrm{beam}},$$

where $F_{\mathrm{beam}} \equiv 1 - \cos\theta_{\mathrm{jet}}$ is the beaming factor, θ_{jet} is the jet opening angle. The uncertainty of E_γ propagates from the uncertainties of $E_{\mathrm{iso\ and}}\ F_{\mathrm{beam}}$.

In order to test if the correlations discussed in the above section vary with redshift, we divide the GRB samples into two subsamples corresponding to the following redshift bins: the low-z sample ($z \leq 1.4$) which consists of 50 GRBs, and the high-z sample ($z > 1.4$) which consists of 66 GRBs. We investigate the redshift dependence of luminosity correlations for this two subsamples, as well as for the full GRBs sample. To fit the six luminosity correlations, we apply the D'Agostini's liklihood[15]

$$\mathcal{L}(\sigma_{\mathrm{int}}, a, b) \propto \prod_i \frac{1}{\sqrt{\sigma_{\mathrm{int}}^2 + \sigma_{yi}^2 + b^2\sigma_{xi}^2}} \times \exp\left[-\frac{(y_i - a - bx_i)^2}{2\left(\sigma_{\mathrm{int}}^2 + \sigma_{yi}^2 + b^2\sigma_{xi}^2\right)}\right]$$

For each correlation and each redshift bin, By maximizing this joint likelihood function, we can derive the best-fitting parameters a, b and the intrinsic scatter σ_{int}, where the intrinsic scatter σ_{int} denotes any other unknown errors except for the measurement errors. The results of the fits and the number of GRBs used in each fit are summarized in (1.1).

Correlation	sample	N	a	a_{err}	b	b_{err}	σ	σ_{int}
$T_{lag} - L$	low-z	37	52.09	0.11	-0.78	0.16	0.51	0.09
	high-z	32	52.59	0.07	-0.65	0.12	0.22	0.09
	All-z	69	52.32	0.07	-0.76	0.11	0.47	0.06
$V - L$	low-z	47	52.1	0.25	0.65	0.37	0.93	0.14
	high-z	57	52.8	0.15	0.34	0.14	0.62	0.07
	All-z	104	52.38	0.14	0.6	0.15	0.76	0.07
$E_{peak} - L$	low-z	50	51.87	0.09	1.47	0.19	0.59	0.07
	high-z	66	52.48	0.06	1.15	0.15	0.3	0.06
	All-z	116	52.17	0.06	1.44	0.14	0.55	0.05
$E_{peak} - E_{\gamma}$	low-z	12	50.63	0.08	1.56	0.19	0.23	0.09
	high-z	12	50.74	0.14	1.17	0.43	0.39	0.14
	All-z	24	50.67	0.07	1.47	0.17	0.26	0.07
$T_{RT} - L$	low-z	39	52.69	0.13	-1.34	0.19	0.48	0.07
	high-z	40	52.86	0.08	-0.81	0.17	0.34	0.07
	All-z	79	52.77	0.08	-1.23	0.13	0.45	0.05
$E_{peak} - E_{iso}$	low-z	40	52.56	0.1	1.6	0.2	0.6	0.08
	high-z	61	53.0	0.06	1.27	0.14	0.38	0.04
	All-z	101	52.8	0.06	1.53	0.13	0.52	0.04

Table 1.1: Best fitting parameters for luminsoity correlations. N is the number of GRB samples.

We perform a Markov Chain Monte Carlo analysis to calculate the posterior probability density function (PDF) of parameter space. We assume a flat prior on all the free parameters and limit $\sigma_{\rm int} > 0$. Note that not all GRBs can be used to analyze each luminosity correlation, because not all the necessary quantities are measurable for some GRBs. For example, GRBs without measurement of the spectrum lag can not used in the $\tau_{\rm lag} - L$ analysis. Hence, we present the best-fitting parameters, together with the number of available GRBs in each fitting in Table (1.1) In Figure (1.5) we plot all the six luminosity correlations in logarithmic coordinates. Low-z and high-z GRBs are represented by blue and red dots with the error bars denoting 1σ uncertainties. The blue line, red line and black line stand for the best-fitting results for low-z GRBs, high-z GRBs and all-z GRBs, respectively.

As shown in Table (1.1) low-z GRBs have a smaller intercept, but a sharper slope than high-z GRBs for all the six luminosity correlations. All-z GRBs have the parameter values between that of low-z and high-z subsamples. For the intrinsic scatter, low-z GRBs have larger value than high-z GRBs, and the $E_p - E_\gamma$ relation has the smallest intrinsic scatter hence we can only obtain its upper limit. The $V - L$ relation has the largest intrinsic scatter, thus it can not be fitted well with a simple line, which is legible in Figure (1.5). $E_p - E_\gamma$ relation of low-z GRBs is consistent with that of high-z GRBs at 1σ confidence level. For the rest luminosity correlations, however, the intercepts and slopes for low-z GRBs differ from that of high-z GRBs.

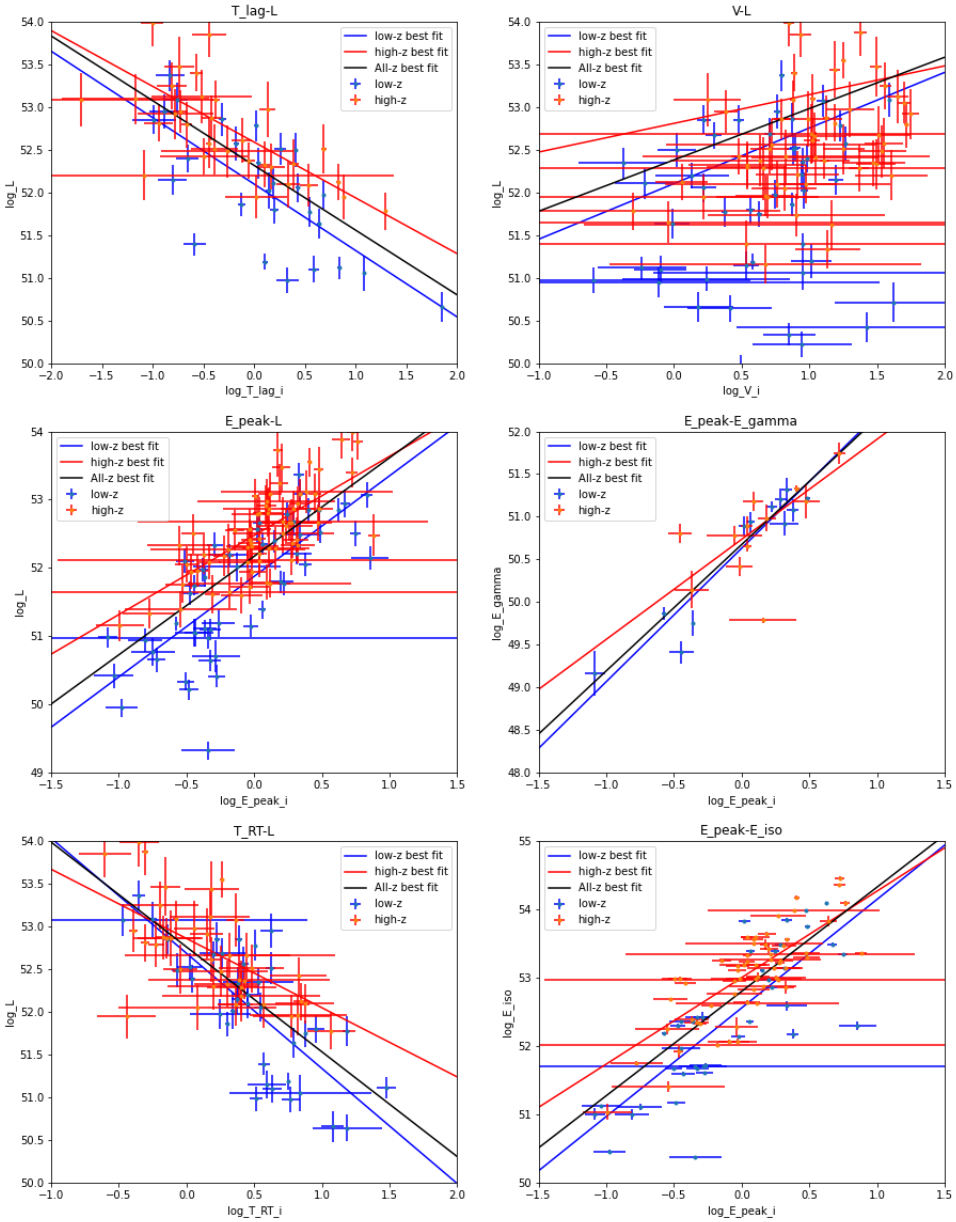

Figure 1.5: Luminsosity correlations best fit

1.5.3 Calibrating distance modulus from $E_{peak} - E_{gamma}$ relation

Having luminosity correlations calibrated, we can conversely using these correlations to calibrate the distance of GRBs, and further use GRBs to constrain cosmological models. Since our calibration of luminosity correlations is independent of cosmological model, the circularity problem is avoided. As we have seen, the $E_p - E_\gamma$ relation is not significantly evolving with redshift, so we use this relation to calibrate the distance of GRBs.

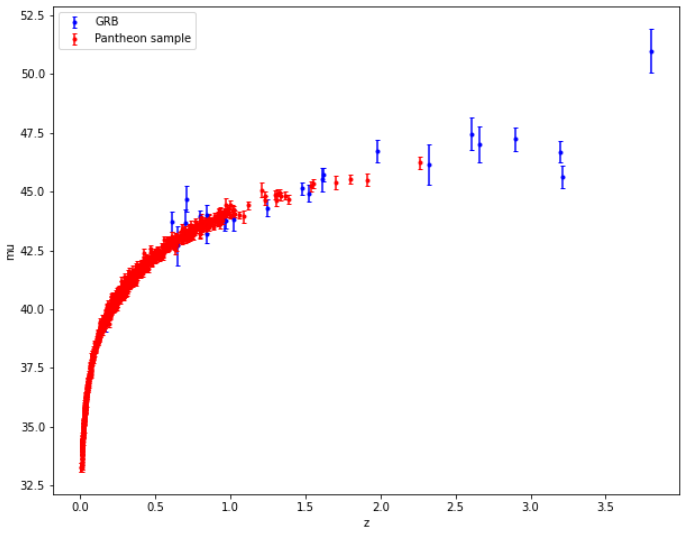

Figure 1.6: GRB Hubble Diagram

1.5.4 Constraints on the dark energy

Luminosity distance can be written as

$$d_L = c(1+z)\int_0^z \frac{1}{H(z)}dz \tag{1.25}$$

For flat ΛCDM, $H(z)$ can be written as

$$H(z) = H_0\sqrt{\Omega_M(1+z)^2 + 1 - \Omega_M} \tag{1.26}$$

We use emcee[16] to fit the dark energy equation. With the Pantheon dataset, the matter density of the flat ΛCDM model is constrained to be $\Omega_M = 0.278 \pm 0.007$. With 24 long GRBs alone, the matter density is constrained to be $\Omega_M = 0.25 \pm 0.15$. It indicates that the Hubble diagram in high redshift is consistent with the ΛCDM model

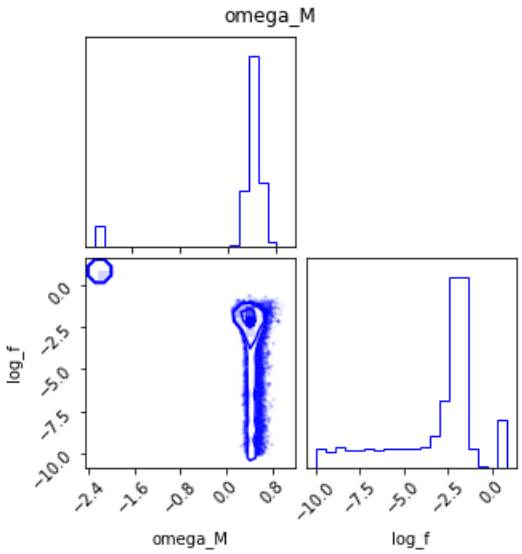

Figure 1.7: GRB Hubble Diagram

1.6 Reconstruction and calibration of distance modulus using Deep Learning

We construct the RNN+BNN network and train it with the package TensorFlow2[17]. For clarity, we present the corresponding hyperparameters and list the steps to reconstruct data with our network as follow: (a) Data processing. The scale of data has an effect on training. Hence, we normalize the distance moduli of the sorted Pantheon data and re-arrange $\mu - z$ as sequences with the step number t = 4. (b) Building RNN. We build RNN with three layers, i.e. an input layer, a hidden layer and an output layer as described in Figure 1. The first two layers are constructed with the LSTM cells of 100 neurons. The redshifts $z_{<t>}$ and the corresponding distance moduli $\mu_{<t>}$ are the input and output vectors, respectively. We employ the Adam optimizer to minimize the cost function MSE and train the network 1000 times. (c) Building BNN. We set the dropout rate to 0 in the input layer to avoid the lost of information, and to 0.2 in the second layer as well as the output layer. We execute the trained network 1000 times to obtain the distribution of distance moduli

1.6.1 Training

We train the neural network using Pantheon data, in which the redshift is the feature and the distance module is the target. The pantheon data is split into train and test data in equal size randomly. 512 datapoints are used for training and remaining for testing. The network architecture is described in previous section. We use mean squared error(MSE) loss and Adam[18] optimizer, with early stopping technique to prevent overfitting. Dropout technique with dropout_rate = 0.2. The hyperparameters used are batch_size = 10, learning_rate = 1e-3, patience = 5.

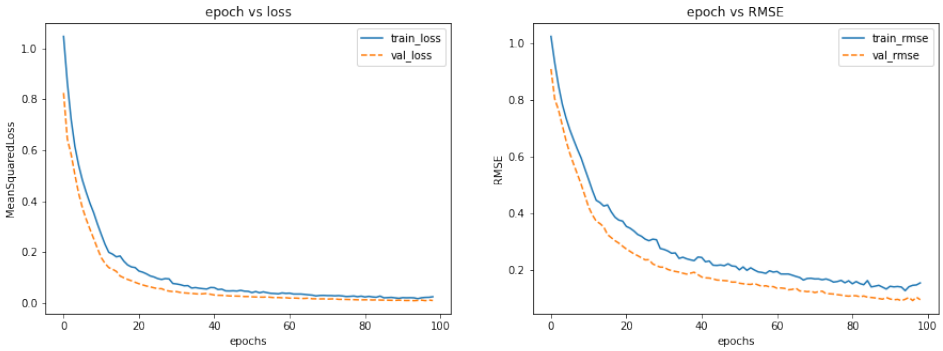

Figure 1.8: Loss curve

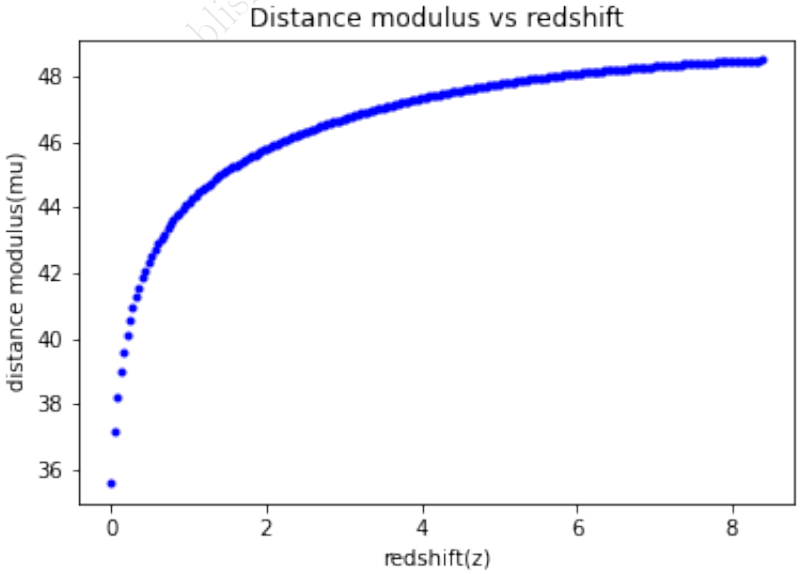

Figure 1.9: Loss curve

1.6.2 Testing redshift dependence of luminosity correlations

Correlation	sample	N	a	a_{err}	b	b_{err}	σ	σ_{int}
$T_{lag} - L$	low-z	37	52.1	0.1	-0.77	0.15	0.49	0.08
	high-z	32	52.37	0.07	-0.6	0.12	0.29	0.07
	All-z	69	52.22	0.06	-0.7	0.1	0.42	0.05
$V - L$	low-z	47	52.12	0.25	0.65	0.36	0.91	0.13
	high-z	57	52.63	0.18	0.25	0.17	0.63	0.07
	All-z	104	52.34	0.13	0.46	0.14	0.75	0.07
$E_{peak} - L$	low-z	50	51.89	0.09	1.43	0.18	0.59	0.07
	high-z	66	52.23	0.05	1.09	0.14	0.34	0.05
	All-z	116	52.05	0.05	1.35	0.12	0.5	0.04
$E_{peak} - E_{\gamma}$	low-z	12	50.66	0.09	1.47	0.2	0.25	0.09
	high-z	12	50.53	0.13	1.37	0.43	0.39	0.16
	All-z	24	50.61	0.06	1.45	0.16	0.25	0.07
$T_{RT} - L$	low-z	39	52.68	0.13	-1.3	0.19	0.48	0.07
	high-z	40	52.61	0.09	-0.74	0.17	0.39	0.06
	All-z	79	52.62	0.07	-1.08	0.12	0.44	0.04
$E_{peak} - E_{iso}$	low-z	40	52.57	0.1	1.55	0.2	0.6	0.08
	high-z	61	52.74	0.06	1.2	0.15	0.4	0.04
	All-z	101	52.65	0.05	1.42	0.12	0.49	0.04

Table 1.2: Best fitting parameters for luminsoity correlations. N is the number of GRB samples.

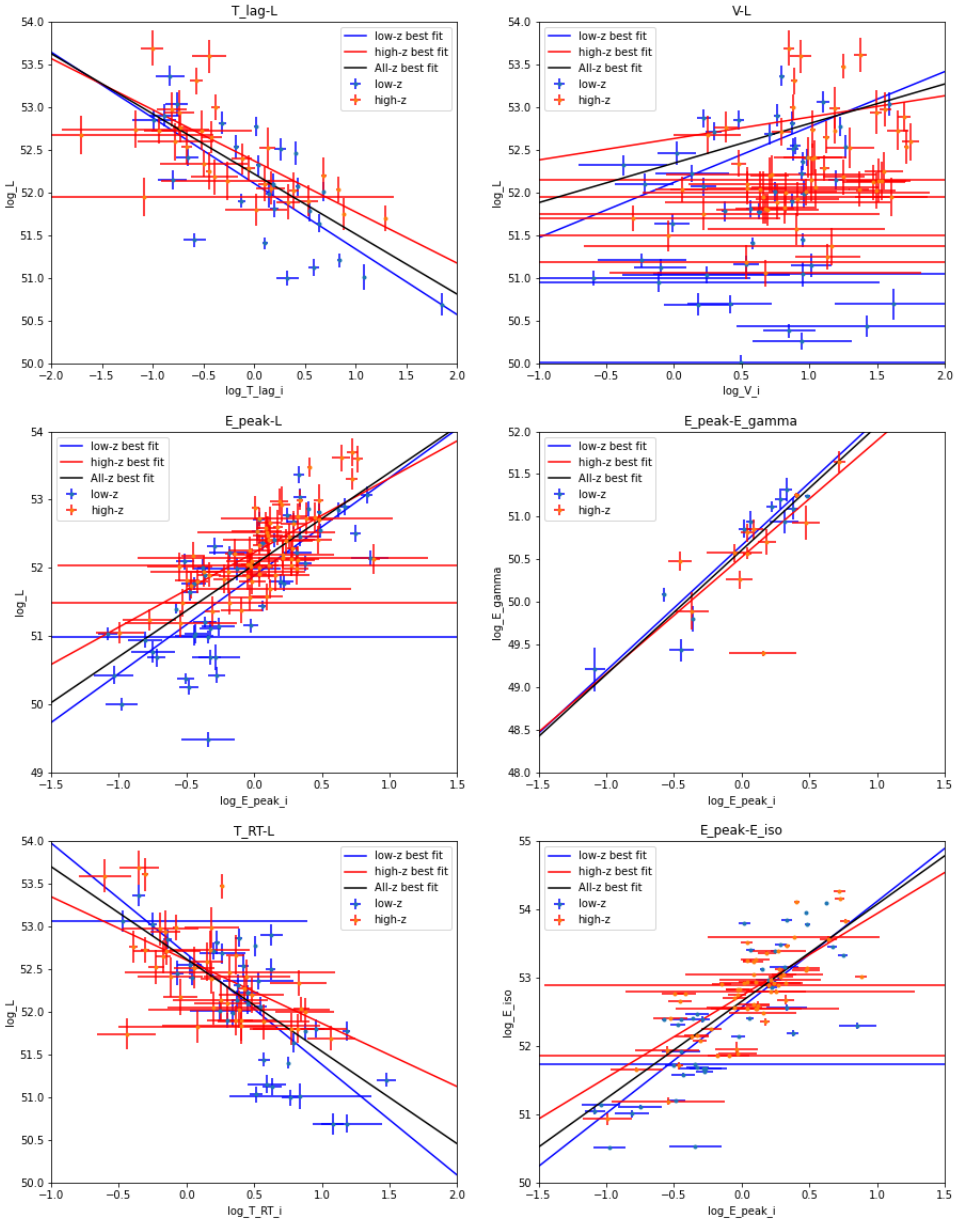

Figure 1.10: Luminsosity correlations best fit

1.6.3 Calibrating distance modulus from $E_{peak} - E_{gamma}$ relation

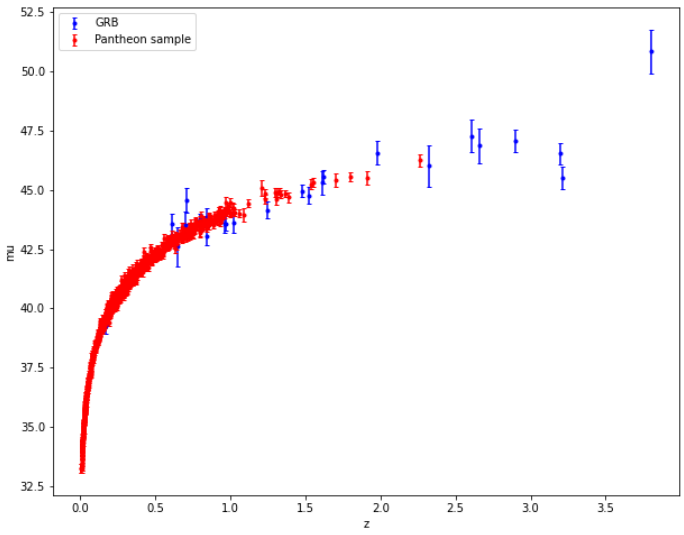

Figure 1.11: GRB Hubble Diagram

1.6.4 Constraints on dark energy

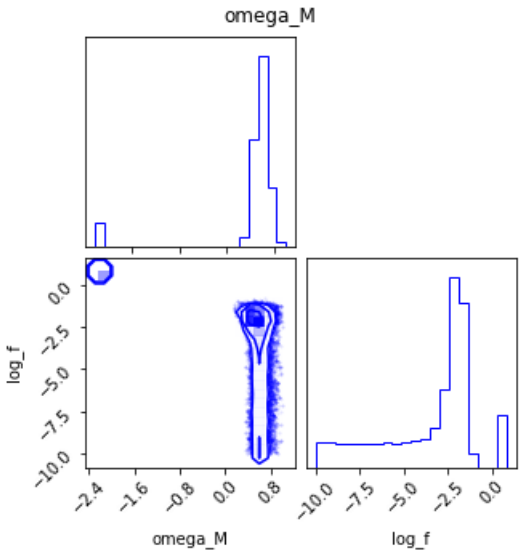

Figure 1.12: GRB Hubble Diagram

1.7 Redoing analysis with Union2.1 Sample

We redo all the analysis done for pantheon with union2.1 data and below are the results. 1.7.1 describes the results of reconstruction from Gaussian Process using Union2.1 dataset. 1.7.2 describes the results of reconstruction from deep learning using Union2.1 dataset.

1.7.1 using Gaussian Processes

Training

The posterior drawn Gaussian process is shown below

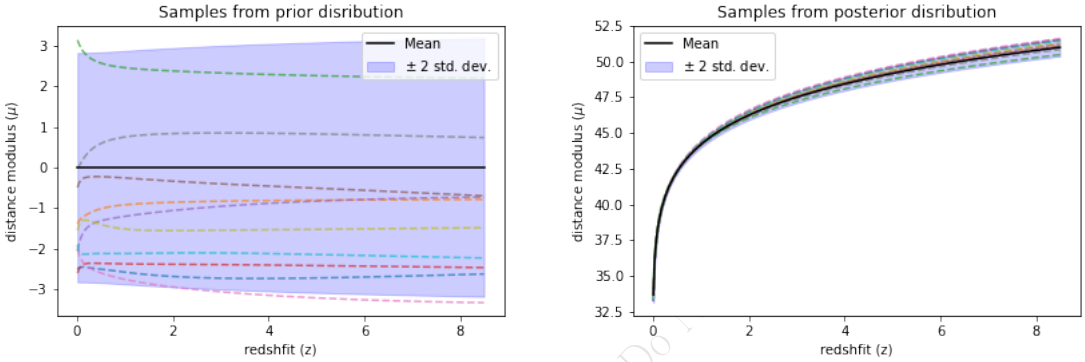

(a) Prior samples drawn from GP (b) Posterior samples drawn from GP

Figure 1.13: Prior and Posterior distrution samples

The error bars with predictions are shown below

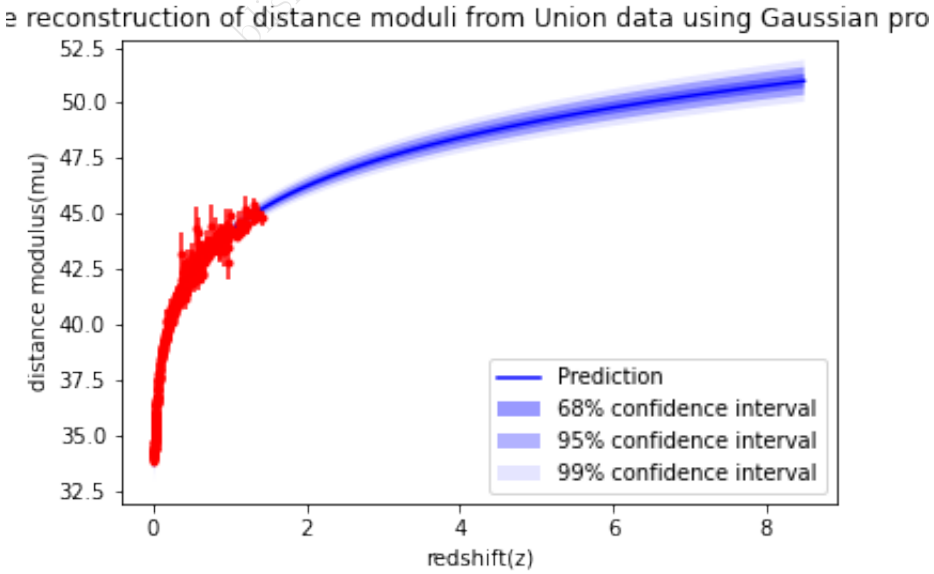

Figure 1.14: Reconstruction from Gaussian Processes

Log Marginal Likelihood = -20.3

Score = 99.51

Testing redshift dependence of luminosity correlations

Correlation	sample	N	a	a_{err}	b	b_{err}	σ	σ_{int}
$T_{lag} - L$	low-z	37	52.13	0.11	-0.79	0.16	0.53	0.08
	high-z	32	52.62	0.07	-0.65	0.12	0.36	0.06
	All-z	69	52.36	0.07	-0.77	0.11	0.5	0.05
$V - L$	low-z	47	52.11	0.25	0.65	0.37	0.93	0.14
	high-z	57	52.83	0.16	0.34	0.15	0.62	0.07
	All-z	104	52.4	0.14	0.6	0.15	0.76	0.07
$E_{peak} - L$	low-z	50	51.9	0.09	1.47	0.19	0.61	0.07
	high-z	66	52.52	0.06	1.13	0.15	0.41	0.04
	All-z	116	52.22	0.06	1.44	0.14	0.58	0.04
$E_{peak} - E_{\gamma}$	low-z	12	50.65	0.08	1.56	0.19	0.24	0.09
	high-z	12	50.76	0.14	1.18	0.42	0.4	0.14
	All-z	24	50.7	0.06	1.48	0.17	0.27	0.07
$T_{RT} - L$	low-z	39	52.71	0.13	-1.34	0.19	0.51	0.07
	high-z	40	52.9	0.08	-0.83	0.18	0.43	0.06
	All-z	79	52.8	0.08	-1.23	0.13	0.49	0.05
$E_{peak} - E_{iso}$	low-z	40	52.58	0.1	1.6	0.2	0.6	0.08
	high-z	61	53.03	0.06	1.28	0.14	0.39	0.04
	All-z	101	52.83	0.06	1.53	0.13	0.52	0.04

Table 1.3: Best fitting parameters for luminsoity correlations. N is the number of GRB samples.

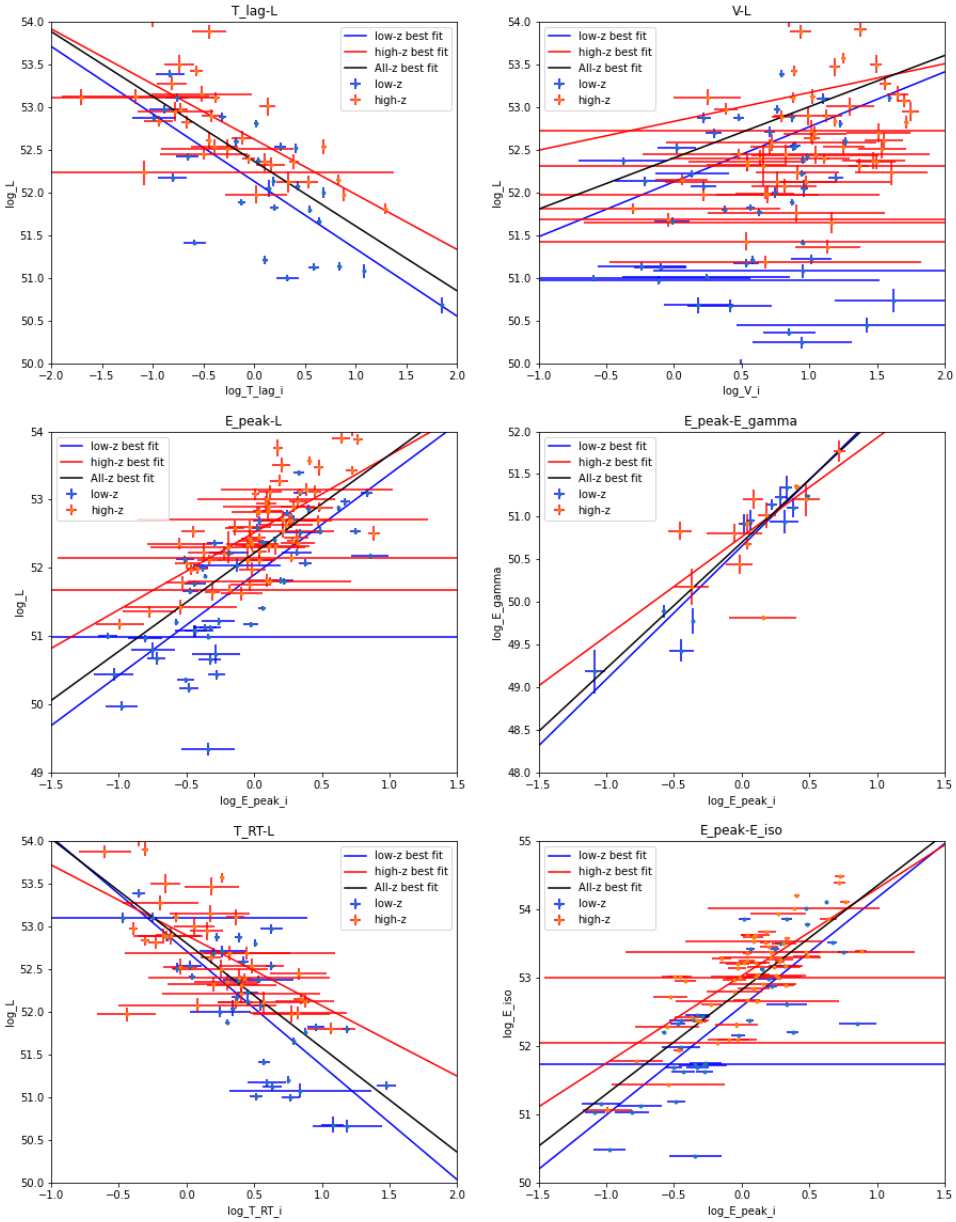

Figure 1.15: Luminsosity correlations best fit

Calibrating distance modulus from $E_{peak} - E_{gamma}$ relation

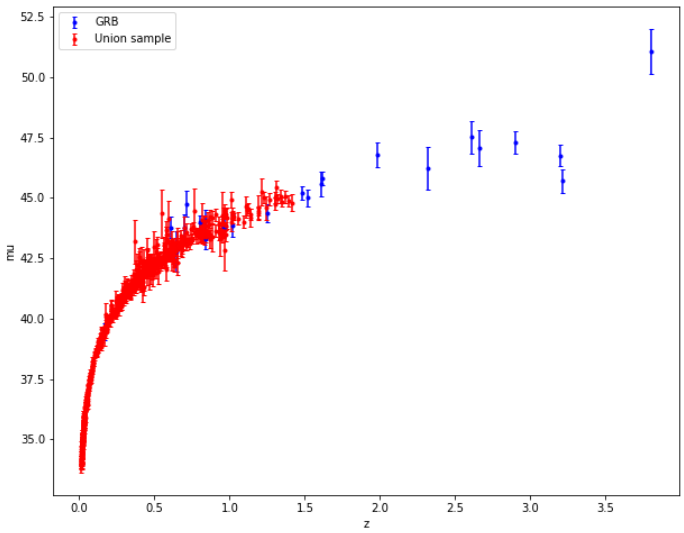

Figure 1.16: GRB Hubble Diagram

Constraints on the dark energy

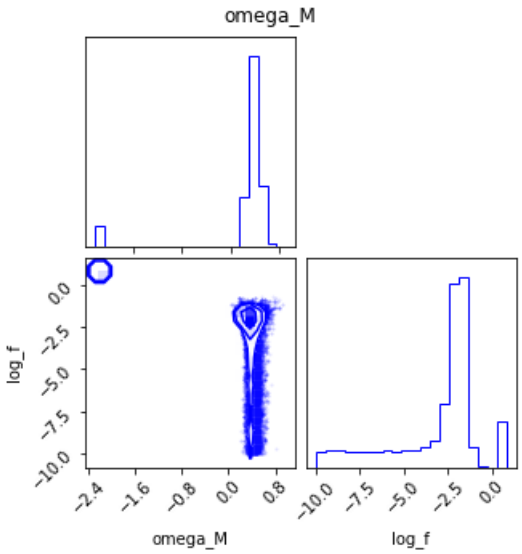

Figure 1.17: GRB Hubble Diagram

1.7.2 using Deep Learning

Training

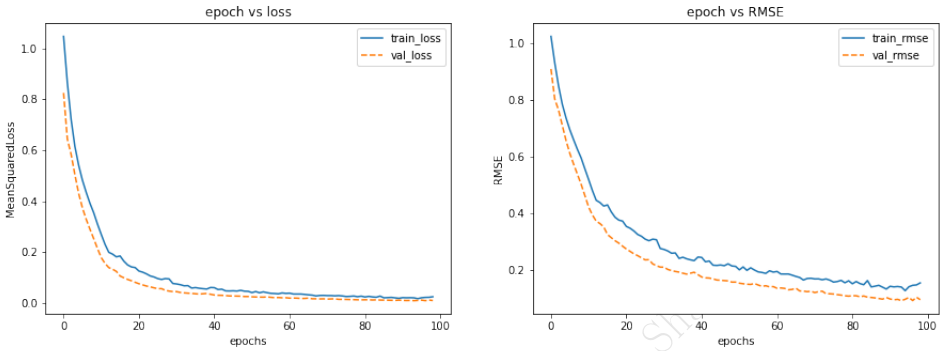

Figure 1.18: Loss curve

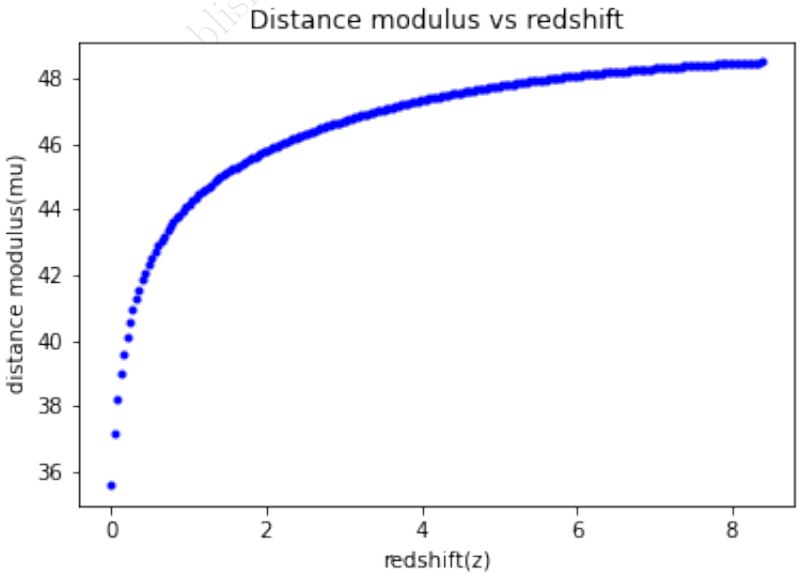

Figure 1.19: Loss curve

Testing redshift dependence of luminosity correlations

Correlation	sample	N	a	a_{err}	b	b_{err}	σ	σ_{int}
$T_{lag} - L$	low-z	37	52.14	0.1	-0.78	0.16	0.51	0.08
	high-z	32	52.18	0.08	-0.51	0.13	0.36	0.07
	All-z	69	52.14	0.06	-0.65	0.1	0.43	0.05
$V - L$	low-z	47	52.14	0.25	0.65	0.37	0.92	0.14
	high-z	57	52.56	0.24	0.1	0.23	0.66	0.07
	All-z	104	52.33	0.14	0.32	0.15	0.79	0.07
$E_{peak} - L$	low-z	50	51.92	0.09	1.46	0.18	0.6	0.07
	high-z	66	52.0	0.06	0.99	0.16	0.4	0.05
	All-z	116	51.95	0.05	1.28	0.12	0.5	0.04
$E_{peak} - E_{\gamma}$	low-z	12	50.67	0.08	1.56	0.18	0.21	0.08
	high-z	12	50.36	0.16	1.57	0.5	0.45	0.18
	All-z	24	50.54	0.07	1.58	0.17	0.28	0.08
$T_{RT} - L$	low-z	39	52.73	0.13	-1.33	0.19	0.48	0.07
	high-z	40	52.39	0.09	-0.63	0.18	0.43	0.06
	All-z	79	52.51	0.07	-0.98	0.12	0.46	0.05
$E_{peak} - E_{iso}$	low-z	40	52.6	0.1	1.6	0.2	0.59	0.08
	high-z	61	52.51	0.07	1.13	0.17	0.47	0.05
	All-z	101	52.53	0.06	1.36	0.13	0.52	0.04

Table 1.4: Best fitting parameters for luminsoity correlations. N is the number of GRB samples.

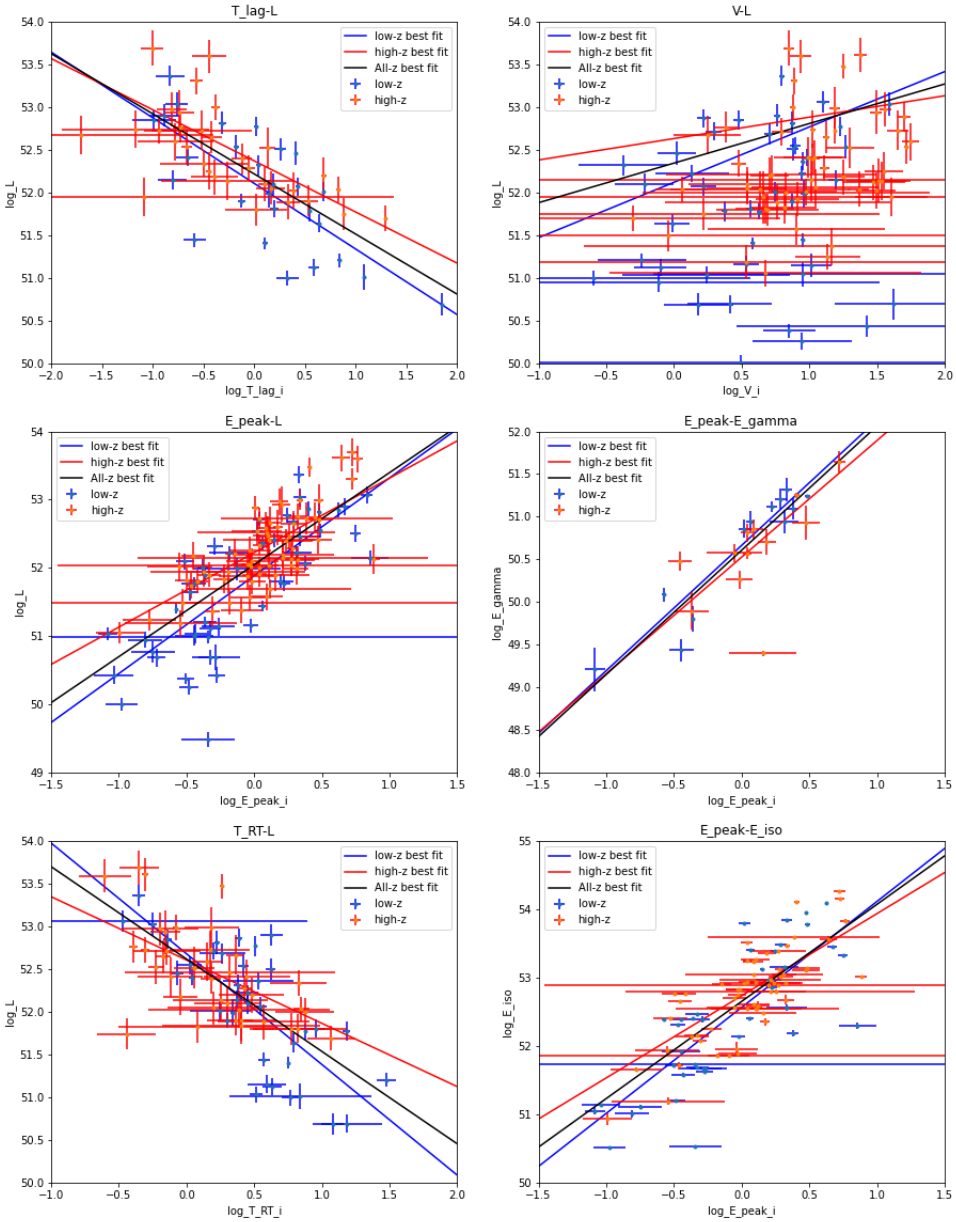

Figure 1.20: Luminsosity correlations best fit

Calibrating distance modulus from $E_{peak} - E_{gamma}$ relation

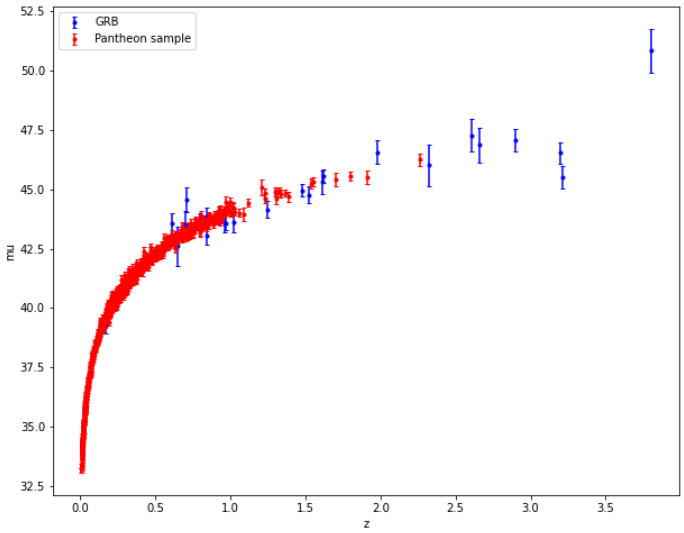

Figure 1.21: GRB Hubble Diagram

Constraints on dark energy

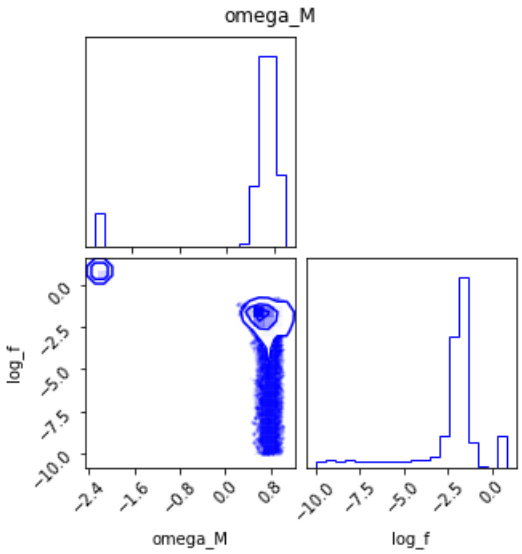

Figure 1.22: GRB Hubble Diagram

1.8 Conclusion

GRB are essential to extend the Hubble Diagram(HD) to higher redshift and study the nature of dark energy in higher redshift. Luminosity distance of GRBs needs to calibrated using luminosity indicators. This calibration depends on the redshift-distance modulus relation. Here explore model independent ways namely, Gaussian Processes and Deep Learning to reconstruct the $/mu-z$ relation, hence avoid circularity problem. We found that not all luminosity correlation are redshift dependent. Specifically $E_{peak} - E_{\gamma}$ relation has no evidence for redshift dependence. Hence we use it calibrate luminosity distance and obtain tight constraints on dark energy parameters.

References

[1] A. G. Riess, A. V. Filippenko, P. Challis, A. Clocchiatti, A. Diercks, P. M. Garnavich, R. L. Gilliland, C. J. Hogan, S. Jha, R. P. Kirshner et al. Observational evidence from supernovae for an accelerating universe and a cosmological constant. *The Astronomical Journal* 116, (1998) 1009.

[2] S. Perlmutter, G. Aldering, G. Goldhaber, R. Knop, P. Nugent, P. G. Castro, S. Deustua, S. Fabbro, A. Goobar, D. E. Groom et al. Measurements of Ω and Λ from 42 high-redshift supernovae. *The Astrophysical Journal* 517, (1999) 565.

[3] B. E. Schaefer. The Hubble diagram to redshift$>$ 6 from 69 gamma-ray bursts. *The Astrophysical Journal* 660, (2007) 16.

[4] L.-X. Li. Variation of the Amati relation with cosmological redshift: a selection effect or an evolution effect? *Monthly Notices of the Royal Astronomical Society: Letters* 379, (2007) L55–L59.

[5] S. Basilakos and L. Perivolaropoulos. Testing gamma-ray bursts as standard candles. *Monthly Notices of the Royal Astronomical Society* 391, (2008) 411–419.

[6] F.-Y. Wang, S. Qi, and Z.-G. Dai. The updated luminosity correlations of gamma-ray bursts and cosmological implications. *Monthly Notices of the Royal Astronomical Society* 415, (2011) 3423–3433.

[7] L. Tang, X. Li, H.-N. Lin, and L. Liu. Model-independently calibrating the luminosity correlations of gamma-ray bursts using deep learning. *The Astrophysical Journal* 907, (2021) 121.

[8] D. M. Scolnic, D. Jones, A. Rest, Y. Pan, R. Chornock, R. Foley, M. Huber, R. Kessler, G. Narayan, A. Riess et al. The complete light-curve sample of spectroscopically confirmed SNe Ia from Pan-STARRS1 and cosmological constraints from the combined pantheon sample. *The Astrophysical Journal* 859, (2018) 101.

[9] N. Suzuki, D. Rubin, C. Lidman, G. Aldering, R. Amanullah, K. Barbary, L. Barrientos, J. Botyanszki, M. Brodwin, N. Connolly et al. The Hubble Space Telescope cluster supernova survey. V. Improving the dark-energy constraints above z$>$ 1 and building an early-type-hosted supernova sample. *The Astrophysical Journal* 746, (2012) 85.

[10] C. E. Rasmussen. Gaussian processes in machine learning. In Summer school on machine learning. Springer, 2003 63–71.

[11] C. Escamilla-Rivera, M. A. C. Quintero, and S. Capozziello. A deep learning approach to cosmological dark energy models. *Journal of Cosmology and Astroparticle Physics* 2020, (2020) 008.

[12] N. Srivastava, G. Hinton, A. Krizhevsky, I. Sutskever, and R. Salakhutdinov. Dropout: a simple way to prevent neural networks from overfitting. *The journal of machine learning research* 15, (2014) 1929–1958.

[13] Y. Gal and Z. Ghahramani. A theoretically grounded application of dropout in recurrent neural networks. *Advances in neural information processing systems* 29.

[14] F. Pedregosa, G. Varoquaux, A. Gramfort, V. Michel, B. Thirion, O. Grisel, M. Blondel, P. Prettenhofer, R. Weiss, V. Dubourg, J. Vanderplas, A. Passos, D. Cournapeau, M. Brucher, M. Perrot, and E. Duchesnay. Scikit-learn: Machine Learning in Python. *Journal of Machine Learning Research* 12, (2011) 2825–2830.

[15] G. D'Agostini. Fits, and especially linear fits, with errors on both axes, extra variance of the data points and other complications. *arXiv preprint physics/0511182* .

[16] D. Foreman-Mackey, D. W. Hogg, D. Lang, and J. Goodman. emcee: The MCMC Hammer. *PASP* 125, (2013) 306–312.

[17] M. Abadi, A. Agarwal, P. Barham, E. Brevdo, Z. Chen, C. Citro, G. S. Corrado, A. Davis, J. Dean, M. Devin, S. Ghemawat, I. Goodfellow, A. Harp, G. Irving, M. Isard, Y. Jia, R. Jozefowicz, L. Kaiser, M. Kudlur, J. Levenberg, D. Mané, R. Monga, S. Moore, D. Murray, C. Olah, M. Schuster, J. Shlens, B. Steiner, I. Sutskever, K. Talwar, P. Tucker, V. Vanhoucke, V. Vasudevan, F. Viégas, O. Vinyals, P. Warden, M. Wattenberg, M. Wicke, Y. Yu, and X. Zheng. TensorFlow: Large-Scale Machine Learning on Heterogeneous Systems 2015. Software available from tensorflow.org.

[18] D. P. Kingma and J. Ba. Adam: A method for stochastic optimization. *arXiv preprint arXiv:1412.6980* .

Chapter 2

Model Comparison of Dark Energy models Using Deep Network

2.1 Introduction

[1] and [2] discovered that luminosity of Type Ia Supernovae are fainter than expected for decelerating Universe. This lead to conclusion that universe expansion is accelerating. Dark energy is proposed to account for this accelerating expansion, and its makes 73% of universe. Other observations from Cosmic Microwave Background(CMB)[**?**] and Baryon Acoustic Oscillations(BAO)[**?**] also supports this claim. The study of the nature of dark energy has become one of the most important issues in the field of fundamental physics. The simplest model for dark energy is ΛCDM, where Λ is the cosmological constant, which is equivalent to the quantum vacuum energy. For ΛCDM, the equation of state parameter is $w = -1$, so $p = -\rho$. ΛCDM model is very popular and accepted, since it can explain the current various astronomical observations quite well. But the cosmological constant has always been facing the severe theoretical challenges, such as the fine-tuning and coincidence problems. Hence other possible models are proposed. For example, a spatially homogeneous, slowly rolling scalar field can also provide a negative pressure, driving the cosmic acceleration[**?**]. More generally, one can phenomenologically characterize the property of dynamical dark energy through parametrizing w of its equation of state (EoS) $p = -w\rho$, where w is usually called the EoS parameter of dark energy. For example, the simplest parametrization model corresponds to the case of $w = constant$, and this cosmological model is sometimes called the ωCDM model. A more physical and realistic situation is that w is time variable, which is often probed by the so-called Chevalliear–Polarski–Linder (CPL) parametrization, $w(a) = w_0 + w_a(1 - a)$ [**?**].

2.2 Literature Survey

Since various dark energy models have been proposed, then the natural question is which model to select given the observational data. A variety of methods such as the $F-$test, Akaike information criterion (AIC), Mallows C_p, Bayesian information criterion (BIC), minimum description length (MDL), and Bayesian model averaging have been proposed to select a good or useful model in light of observations. [**?**] strongly recommends using Bayesian evidence to assign preferences to alternative

models since the evidence is the Bayesian's transportable quantity between models, and the popular easyto use AIC and BIC as well as MDL methods are all approximations to the Bayesian evidence[**?**]. The Bayesian evidence for model selection has been applied to the study of cosmology for a long time ([**?**] [**?**] [**?**], and recently a detailed study of Bayesian evidence for a large class of cosmological models taking into account around 21 different dark energy models has been performed by [**?**]. Although Bayesian evidence remains the preferred method compared with information criterions, a full Bayesian inference for model selection is very computationally expensive and often suffers from multi-modal posteriors and parameter degeneracies, which lead to a large time consumption to obtain the final result. Recently, deep learning models has been proposed for model selection. [**?**] proposed to use VAE−GAN model for both interpolation and model selection.

2.3 Observational Data

2.3.1 Union2.1

The observations are from the Union2.1 compilation [9] which contains 580 SNeIa, and $\boldsymbol{x}_{obs,\,\mathrm{real}}$ signify the measured distance moduli, Σ_{obs} represents the covariance of the distance moduli with systematics.

2.4 Methodology

2.4.1 VAE

A VAE[**?**] consists of two networks that encode a data sample x to a latent representation z and decode the latent representation back to data space, respectively:

$$z = Enc(x) = q(z|x), x' \approx Dec(z) = p(x|z) \tag{2.1}$$

The VAE regularizes the encoder by imposing a prior over the latent distribution $p(z)$. Typically $z \approx N(0, I)$ is chosen. The VAE loss is minus the sum of the expected log likelihood (the reconstruction error) and a prior regularization term:

$$L_{VAE} = -\mathbb{E}_q \left[log \frac{p(x|z)p(z)}{q(z|x)} \right] = L_{like} + L_{prior} \tag{2.2}$$

with

$$L_{like} = -\mathbb{E} \left[log \frac{p(x|z)}{} \right] \tag{2.3}$$

$$L_{prior} = -D_{KL} \left(q(z|x) || p(z) \right) \tag{2.4}$$

where D_{KL} is the Kullback-Leibler divergence

2.4.2 GAN

A GAN[?] consists of two networks: the generator network $Gen(z)$ maps latents z to data space while the discriminator network assigns probability $y = Dis(x) \in [0, 1]$ that x is an actual training sample and probability $1 - y$ that x is generated by our model through $x = Gen(z)$ with $z \approx p(z)$. The GAN objective is to find the binary classifier that gives the best possible discrimination between true and generated data and simultaneously encouraging Gen to fit the true data distribution. We thus aim to maximize/minimize the binary cross entropy:

$$L_{GAN} = log(Dis(x)) + log(1 - Dis(Gen(z))) \tag{2.5}$$

with respect to Dis/Gen with x being a training sample and $z \approx p(z)$.

2.4.3 VAEGAN

[?] proposes a combination of VAE and GAN, that outperforms traditional VAEs. A property of GAN is that its discriminator network implicitly has to learn a rich similarity metric for inputs, so as to discriminate them from generated data. They exploit this observation so as to transfer the properties of input learned by the discriminator into a more abstract reconstruction error for the VAE. The end result will be a method that combines the advantage of GAN as a high quality generative model and VAE as a method that produces an encoder of data into the latent space z.

Specifically, since element-wise reconstruction errors are not adequate for images and other signals with invariances, we propose replacing the VAE reconstruction (expected log likelihood) error term from Eq. 3 with a reconstruction error expressed in the GAN discriminator. To achieve this, let $Dis_l(x)$ denote the hidden representation of the lth layer of the discriminator. We introduce a Gaussian observation model for $Dis_l(x)$ with mean $Dis_l(x')$ and identity covariance:

$$p(Dis_l(x)|z) = N(Dis_l(x)|Dis_l(x'), I) \tag{2.6}$$

where $x' \approx Dec(z)$ is the sample from the decoder of x. We can now replace the VAE error of Eq. 3 with

$$L_{llike}^{Dis_l} = -E_{q(z|x)}[logp(Dis_l(x)|z)] \tag{2.7}$$

We train our combined model with the triple criterion

$$L = L_{prior} + L_{llike}^{Dis_l} + L_{GAN} \tag{2.8}$$

Notably, we optimize the VAE wrt. L_{GAN} which we regard as a style error in addition to the reconstruction error which can be interpreted as a content error using the terminology from Gatys et al. (2015). Moreover, since both Dec and Gen map from z to x, we share the parameters between the two (or in other words, we use Dec instead of Gen in Eq. 5). In practice, we have observed the devil in the details during development and training of this model. We therefore provide a list of practical considerations in this section. We refer to Fig. 2 and Alg. 1 for overviews of the training procedure. To be written

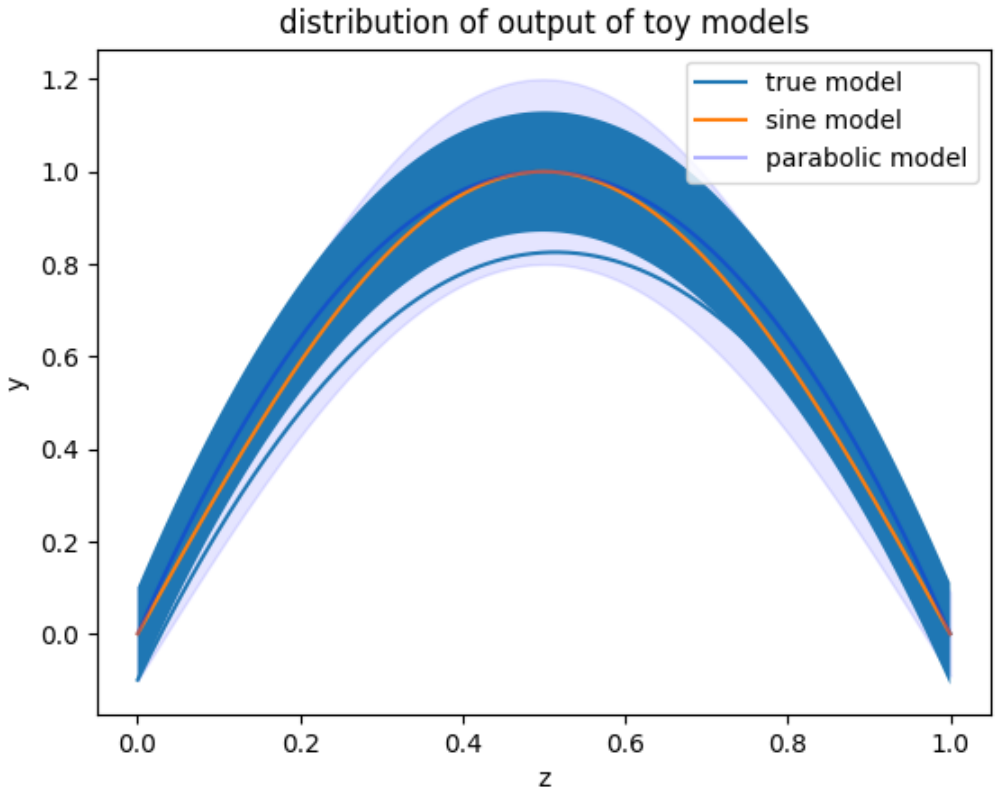

Figure 2.1: Toy models

2.5 Test on toy model

This section creates two toy models to test the data reconstruction and model comparison ability of the network.

Model 1,

$$y = Az^2 + (-A + B)z + C$$
$$\text{where, } A \sim \mathcal{N}(-4, 0.1), B \sim \mathcal{N}(0, 0.01), C \sim \mathcal{N}(0, 0.1)$$

Model 2,

$$y = A\sin(\omega z) + C$$
$$\text{where, } A \sim \mathcal{N}(1, 0.1), \omega \sim \mathcal{N}(\pi, 0.01), C \sim \mathcal{N}(0, 0.1)$$

Model 1 and Model 2 have similar distributions as shown in Figure 2 Given the observations $\boldsymbol{x}_{\text{obs,real}}$ which are generated by the underlying model $y_{\text{true}} = -3.5z^2 + 3.6z - 0.1$ on $\boldsymbol{z}_{\text{obs}} = \{z_1, z_2, \cdots, z_{580}\}$ with an error matrix Σ_{obs}, we would like to fit the two toy models to the observations to tell which one is most probable to be the true model, and interpolate the data with the model at $\boldsymbol{z}^* = \{z_1^*, \cdots, z_M^*\}$, for example, $\boldsymbol{z}^*$ even staying in the interval $[0, 1]$ with $M = 1468$.

First we concatenate and sort $\boldsymbol{z}$ and $\boldsymbol{z}^*$, and call the new one $\boldsymbol{z}$. Then sample $\{A_i, B_i, C_i, \omega_i\}$ from the priors of the toy models and generate the training samples $\boldsymbol{x}_i = M_k(\boldsymbol{z} \mid A_i, B_i, C_i, \omega_i)$ (Note that which set of parameters should be used depends on the toy model). Here 12800 samples

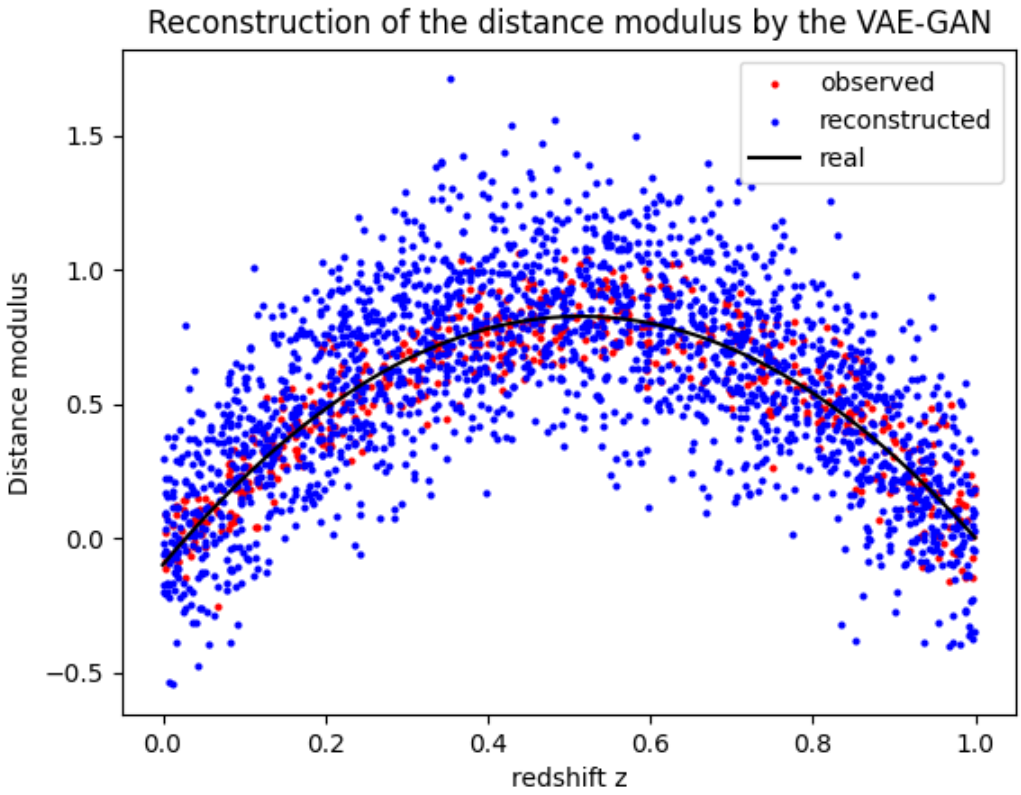

Figure 2.2: Reconstruction

for each model are generated as the training dataset. Finally, the training set $\{\boldsymbol{x}\}_{i=1}^{25600}$ together with the observation error Σ_{obs} is fed into the network. Once the training converges, one can put the observations $\boldsymbol{x}_{obs,real}$ into the network to tell which toy model is most probable and get the interpolation, see Figure 3 In this task, the discriminator has a classification accuracy of almost 1. It assigns a probability of 97% to the parabolic model (Model 1), which is indeed the case.

2.6 Dark enrgy models

We consider three popular dark energy models to test out VAE-GAN network for model selection and interpolation.

2.6.1 ΛCDM

The equation of state parameter is

$$\omega(z) = -1 \tag{2.9}$$

2.6.2 ωCDM

$$\omega(z) = \omega_{DE} \tag{2.10}$$

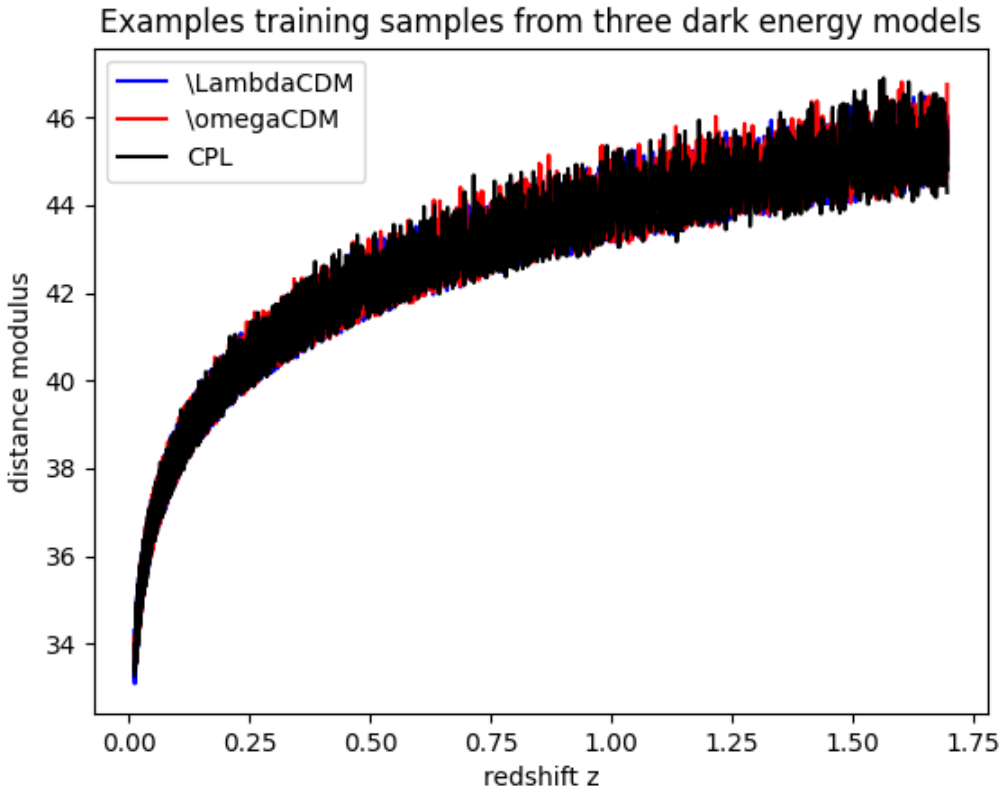

Figure 2.3: Samples from dark energy models

2.6.3 CPL

$$\omega(z) = \omega_0 + \omega_a \frac{z}{1+z} \tag{2.11}$$

2.6.4 Distance Modulus

We evaluate these models at redshifts z_{obs} given by Union2.1 data and randomly sampled redshifts between $(0.8min(z_{obs}) - 1.2 * max(z_{obs})$. The expansion rate of a spatially flat FRW universe is determined by the matter and dark energy,

$$H^2(z) = H_0^2 \left\{ \Omega_{m0}(1+z)^3 + (1-\Omega_{m0}) \exp\left[3 \int \frac{1+\omega\left(z'\right)}{1+z'} dz' \right] \right\}$$

The luminosity distance is closely related to the Hubble expansion rate (Eq.12), and the distance modulus is given by Eq13

$$D_L(z) = c(1+z) \int_0^z dz' \frac{1}{H\left(z'\right)}$$

$$\mu(z) = 5 \log_{10} D_L(z) + 25$$

For each dark energy model, 12800 samples are generated at the redshift $\boldsymbol{z} = \mathrm{sort}\left\{\boldsymbol{z}_{\mathrm{obs}}, \boldsymbol{z}^*\right\}$, given the priors of the parameters as,

$$\begin{aligned} \Omega_{m0} &\sim \mathcal{U}(0.1, 0.9) \\ H_0 &\sim \mathcal{U}(50, 90) \\ \omega_{DE} &\sim \mathcal{U}(-1.8, -0.4) \\ \omega_0 &\sim \mathcal{U}(-1.9, -0.4) \\ \omega_a &\sim \mathcal{U}(-4.0, 4.0) \end{aligned}$$

$\boldsymbol{z}^*$ has 1468 elements evenly located in the interval, $[0.8 \min\left(\boldsymbol{z}_{obs}\right), 1.2 \max\left(\boldsymbol{z}_{obs}\right)]$. The 12800×3 samples

2.7 Conclusion

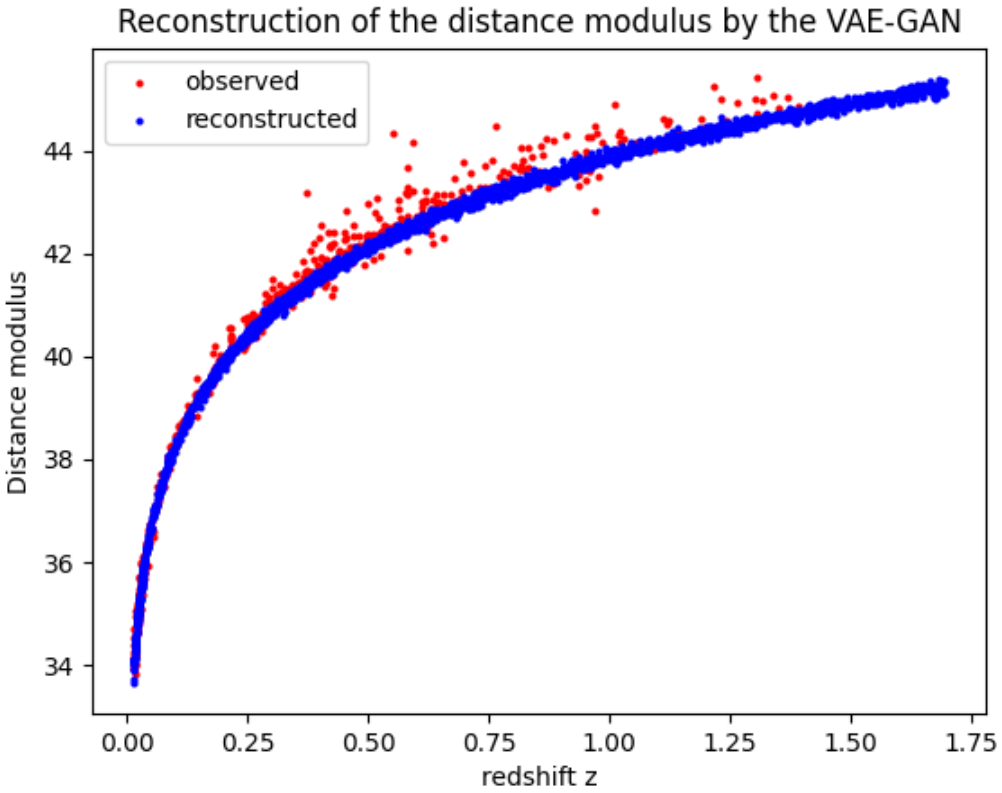

Figure 2.4: Reconstruction

References

[1] A. G. Riess, A. V. Filippenko, P. Challis, A. Clocchiatti, A. Diercks, P. M. Garnavich, R. L. Gilliland, C. J. Hogan, S. Jha, R. P. Kirshner et al. Observational evidence from supernovae for an accelerating universe and a cosmological constant. *The Astronomical Journal* 116, (1998) 1009.

[2] S. Perlmutter, G. Aldering, G. Goldhaber, R. Knop, P. Nugent, P. G. Castro, S. Deustua, S. Fabbro, A. Goobar, D. E. Groom et al. Measurements of Ω and Λ from 42 high-redshift supernovae. *The Astrophysical Journal* 517, (1999) 565.

[3] B. E. Schaefer. The Hubble diagram to redshift$>$ 6 from 69 gamma-ray bursts. *The Astrophysical Journal* 660, (2007) 16.

[4] L.-X. Li. Variation of the Amati relation with cosmological redshift: a selection effect or an evolution effect? *Monthly Notices of the Royal Astronomical Society: Letters* 379, (2007) L55–L59.

[5] S. Basilakos and L. Perivolaropoulos. Testing gamma-ray bursts as standard candles. *Monthly Notices of the Royal Astronomical Society* 391, (2008) 411–419.

[6] F.-Y. Wang, S. Qi, and Z.-G. Dai. The updated luminosity correlations of gamma-ray bursts and cosmological implications. *Monthly Notices of the Royal Astronomical Society* 415, (2011) 3423–3433.

[7] L. Tang, X. Li, H.-N. Lin, and L. Liu. Model-independently calibrating the luminosity correlations of gamma-ray bursts using deep learning. *The Astrophysical Journal* 907, (2021) 121.

[8] D. M. Scolnic, D. Jones, A. Rest, Y. Pan, R. Chornock, R. Foley, M. Huber, R. Kessler, G. Narayan, A. Riess et al. The complete light-curve sample of spectroscopically confirmed SNe Ia from Pan-STARRS1 and cosmological constraints from the combined pantheon sample. *The Astrophysical Journal* 859, (2018) 101.

[9] N. Suzuki, D. Rubin, C. Lidman, G. Aldering, R. Amanullah, K. Barbary, L. Barrientos, J. Botyanszki, M. Brodwin, N. Connolly et al. The Hubble Space Telescope cluster supernova survey. V. Improving the dark-energy constraints above z$>$ 1 and building an early-type-hosted supernova sample. *The Astrophysical Journal* 746, (2012) 85.

[10] C. E. Rasmussen. Gaussian processes in machine learning. In Summer school on machine learning. Springer, 2003 63–71.

[11] C. Escamilla-Rivera, M. A. C. Quintero, and S. Capozziello. A deep learning approach to cosmological dark energy models. *Journal of Cosmology and Astroparticle Physics* 2020, (2020) 008.

[12] N. Srivastava, G. Hinton, A. Krizhevsky, I. Sutskever, and R. Salakhutdinov. Dropout: a simple way to prevent neural networks from overfitting. *The journal of machine learning research* 15, (2014) 1929–1958.

[13] Y. Gal and Z. Ghahramani. A theoretically grounded application of dropout in recurrent neural networks. *Advances in neural information processing systems* 29.

[14] F. Pedregosa, G. Varoquaux, A. Gramfort, V. Michel, B. Thirion, O. Grisel, M. Blondel, P. Prettenhofer, R. Weiss, V. Dubourg, J. Vanderplas, A. Passos, D. Cournapeau, M. Brucher, M. Perrot, and E. Duchesnay. Scikit-learn: Machine Learning in Python. *Journal of Machine Learning Research* 12, (2011) 2825–2830.

[15] G. D'Agostini. Fits, and especially linear fits, with errors on both axes, extra variance of the data points and other complications. *arXiv preprint physics/0511182* .

[16] D. Foreman-Mackey, D. W. Hogg, D. Lang, and J. Goodman. emcee: The MCMC Hammer. *PASP* 125, (2013) 306–312.

[17] M. Abadi, A. Agarwal, P. Barham, E. Brevdo, Z. Chen, C. Citro, G. S. Corrado, A. Davis, J. Dean, M. Devin, S. Ghemawat, I. Goodfellow, A. Harp, G. Irving, M. Isard, Y. Jia, R. Jozefowicz, L. Kaiser, M. Kudlur, J. Levenberg, D. Mané, R. Monga, S. Moore, D. Murray, C. Olah, M. Schuster, J. Shlens, B. Steiner, I. Sutskever, K. Talwar, P. Tucker, V. Vanhoucke, V. Vasudevan, F. Viégas, O. Vinyals, P. Warden, M. Wattenberg, M. Wicke, Y. Yu, and X. Zheng. TensorFlow: Large-Scale Machine Learning on Heterogeneous Systems 2015. Software available from tensorflow.org.

[18] D. P. Kingma and J. Ba. Adam: A method for stochastic optimization. *arXiv preprint arXiv:1412.6980* .

Chapter 3

Photometric redshift estimation using Symbolic Regression

3.1 Introduction

Large scale structure cosmology and extragalactic astronomy rely heavily on accurate estimate of the redshift of objects under study. For example the reconstruction of the two point correlation function for galaxies is critical to understand the history of structure formation in the Universe and probe theories beyond ΛCDM. Unfortunately it is a very time consuming and expensive task to obtain spectroscopic data for the millions of observed galaxies. It has therefore long been a challenge to estimate the redshift of galaxies using the much easier to obtain photometric data.

3.2 Literature Survey

The estimation of redshifts from photometric data has been an industry for some years in astronomy culminating in the production of MegaZ-LRG [**?**], a database of photometric redshifts of 1 million luminous red galaxies in the range $0.4 < z < 0.7$ and the 2MPZ database[**?**] for $z < 0.3$. The aim is to model the spectroscopic redshift using photometric redshift estimator, z_{phot}(u, g, r, i, z), where u, g, r, i, z are the standard photometric magnitudes. There have been two main approaches to the problem: template based methods ([**?**] [**?**] [**?**] [**?**] [**?**] [**?**] [**?**] [**?**] [**?**] [**?**]) and machine learning/empirical methods ([**?**] [**?**] [**?**] [**?**] [**?**] [**?**] [**?**]). For comparisons of the various codes see ([**?**] [**?**] [**?**]). One of the best performing codes is ANNz[**?**] which is based on artificial neural networks and was used in creating the MegaZ and 2MPZ databases.[**?**] proposes non-linear regression with genetic optimization.

3.3 Observation Data

The data in this study are drawn from SDSS Data Release 17 [**?**]. The SDSS I-III uses a 4 meter telescope at Apache Point Observatory in New Mexico and has CCD wide field photometry in 5 bands (u, g, r, i, z [**?**] [**?**]), and an expansive spectroscopic follow up program [**?**] covering π radians of the northern sky. The SDSS collaboration has obtained approximately 2 million galaxy spectra using

dual fiberfed spectrographs. An automated photometric pipeline performed object classification to a magnitude of $r \approx 22$ and measured photometric properties of more than 100 million galaxies. The complete data sample, and many derived catalogs such as the photometric redshift estimates, are publicly available through the CasJobs server[**?**] [1].

3.3.1 SDSS DR17 photometry

The SDSS is well suited to the analysis presented in this paper due to the enormous number of photometrically selected galaxies with spectroscopic redshifts to use as training, cross-validation and test samples. We select 1,958,727 galaxies from CasJobs with both spectroscopic redshifts and photometric properties. In detail we run the following MySQL query in the DR17 schema:

```
-- Goto http://skyserver.sdss.org/casjobs/, create an account run the following sql query
-- http://skyserver.sdss.org/dr17/SearchTools/sql cannot be used to bulk data (only 500000)
-- SQL qeury
-- =========
-- only select galaxies that have a photometric galaxy classification type = 3,
-- and spectscopic redshifts, r band magnitudes, -- and radii greater than 0
-- make a magnitude error cut of < 0.3 (in all 5 bands) to ensure that you don't get junk obje
-- dered_ is simplified mag, corrected for extinction: modelMag - extinction



SELECT
    q.dered_u as u, q.dered_g as g, q.dered_r as r,
    q.dered_i as i, q.dered_z as z, q.modelMagErr_u as u_err,
    q.modelMagErr_g as g_err, q.modelMagErr_r as r_err,
    q.modelMagErr_i as i_err, q.modelMagErr_z as z_err,
    s.z AS specz, s.zerr AS specz_err,
    p.z AS photoz, p.zerr AS photoz_err
INTO mydb.specPhotoDR10v2 FROM
SpecPhotoAll AS s JOIN photoObjAll AS q ON s.objid=q.objid
AND q.dered_u>0
AND q.dered_g>0
AND q.dered_r>0
AND q.dered_z>0
AND q.dered_i>0
AND q.expAB_r>0
AND q.modelMagErr_u < 0.3
AND q.modelMagErr_g < 0.3
AND q.modelMagErr_r < 0.3
AND q.modelMagErr_i < 0.3
AND q.modelMagErr_z < 0.3
```

[1] http://skyserver.sdss.org/casjobs/

```
AND q.type=3
AND s.z > 0
--AND s.zerr > -0.3 AND s.zerr < 0.3
--AND q.petroRad_u > 0 -- has no effect
--AND q.petroRad_g > 0
--AND q.petroRad_r > 0
--AND q.petroRad_i > 0
--AND q.petroRad_z > 0
AND q.CLEAN=1  -- Clean photometry flag
-- (1=clean, 0=unclean)
AND s.zWarning = 0  -- Bitmask of warning
-- vaules; 0 means all
-- is well
LEFT OUTER JOIN Photoz AS p ON s.objid=p.objid
```

We apply the SDSS extinction corrections to the psf and fiber magnitudes, and further only select galaxies that have a photometric galaxy classification type = 3, have spectroscopic redshifts, r band magnitudes, and radii greater than zero. This reduces the sample size to 1,922,231 galaxies.

3.4 Methodology

3.4.1 Symbolic Regression

Symbolic regression (SR) is a novel machine-learning technique that approximates the relation between an input and an output through analytic mathematical formulae ([?] [?] [?] [?] [?] [?] [?]). The advantage of using SR over other ML regression models like RF or deep neural networks is that it provides analytic expressions that can be readily generalized and that facilitate understanding the underlying physics. Furthermore, SR is shown to outperform other ML models when the size of dataset is small[?].

3.5 Photometric redshift estimation

For our symbolic regression we rely on PySR[?]. It uses genetic programming to find a symbolic expression for a numerically defined function in terms of pre-defined variables. The population consists of symbolic expressions, visualized as a tree and consisting of nodes with an operator function or an operand. We use the operators for addition, subtraction, multiplication. The tree population evolves when new individuals are created and old ones are discarded. To breed the next generation, several mutation operators can be applied, for instance exchanging, adding or deleting nodes of the parent tree. The hyperparameter populations = 30 defines the number of populations and is per default set to the number of processors used (procs). The number of individuals per populations is given by npop = 1000. As the figure of merit for the PySR algorithm we take the mean squared

error between the data points $t_i(x, z|\theta)$ and the functional description g_i

$$MSE = \frac{1}{n}\sum_{i=1}^{n}\left(g_i\left(x\right) - t_i(x, z|\theta)\right) \tag{3.1}$$

and balance it with the function's complexity, defined as

$$complexity = \#nodes \tag{3.2}$$

For the PySR score value, not to be confused with the statistics version of the optimal observable defined in, the parameter parsimony balances the two conditions,

$$score = \frac{MSE}{baseline} + parsimony \times complexity \tag{3.3}$$

The normalization factor baseline is the MSE between the data and the constant unit function. The hyperparameter *maxsize* restricts the complexity to a maximum value. We adjust this value depending on the difficulty of the regression task taking 50 as a starting point and increase (decrease) it if the required complexity is larger (smaller). Additionally we can restrict the complexity of specific operators to obtain a more readable result. We set the maximal complexity of square to 5 and cube to 3. Note that in some instances we choose to not extract the score, but the score scaled by a constant, to improve the numerics with an order-one function. Simulated annealing allows us to search for a global optimum in a high-dimensional space while preventing the algorithm from being stuck in a local optimum. A mutation is accepted with the probability

$$p = exp\left(-\frac{score_{new} - score_{old}}{alpha \times T}\right) \tag{3.4}$$

The parameter T is referred to as temperature. It linearly decreases with each cycle or generation, starting with 1 in the first cycle and 0 in the last. The hyperparameter ncyclesperiterations = 200 sets the amount of cycles. We choose alpha = 1. If the new function describes the data better than the reference tree, $score_{new}$ $score_{old}$, the exponent has a positive sign and the new function is accepted. If the new sore is larger than the old score, the acceptance of the new function is given by p and hence exponentially suppressed. We use this default PySR form for our simple example and discuss a bettersuited form for our application in Sec. 3. The hyperparameter niterations = 300 defines the number of iterations of a full simulated annealing process. After each iteration the best formulas are compared to the hall of fame (HoF). For each complexity the best equation is chosen and saved in the output file. An equation of higher complexity is only added if its MSE is smaller than for previous formulas. Equations from different populations or the hall of fame can migrate to other populations. This process is affected by the parameters fractionReplaced = 0.5 and fractionReplacedHof = 0.2.

3.6 Conclusion

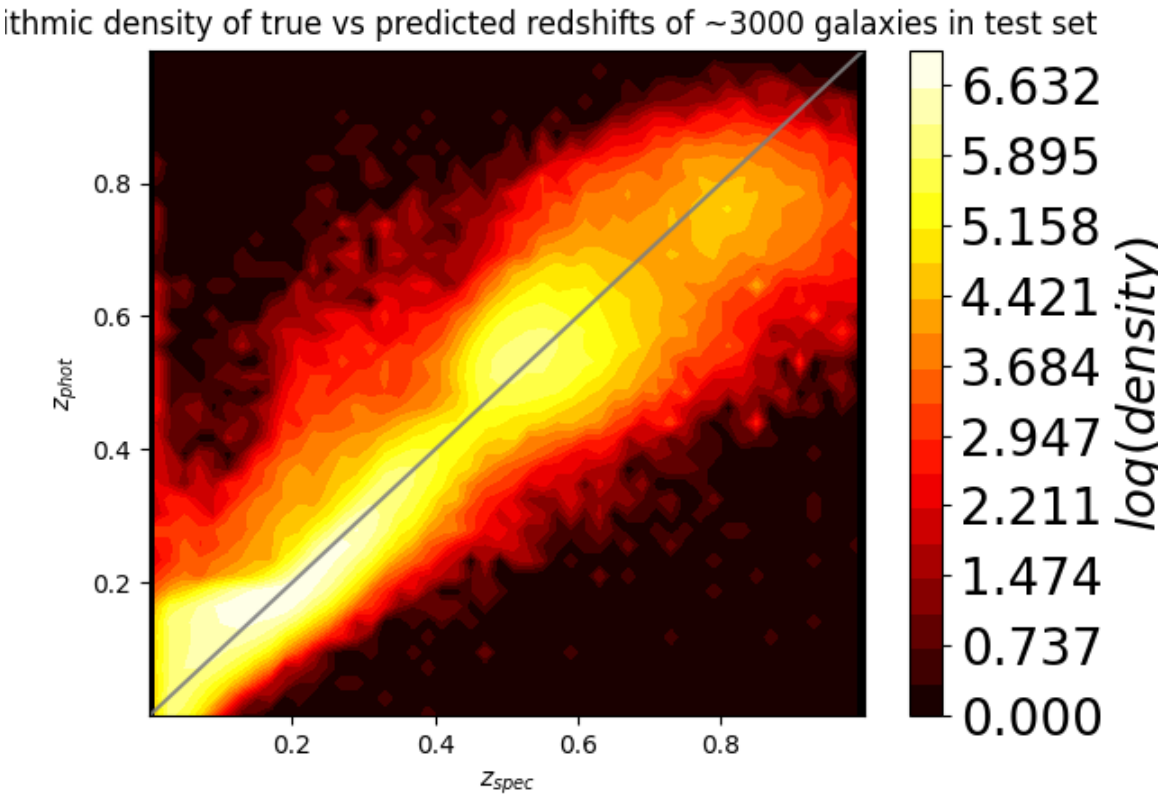

Figure 3.1: Photometric redshift prediction and errorbars for a representative subsample of 300 galaxies. The errorbars are due to errors in the photometric data and so depend on the particular model chosen for z_{phot}

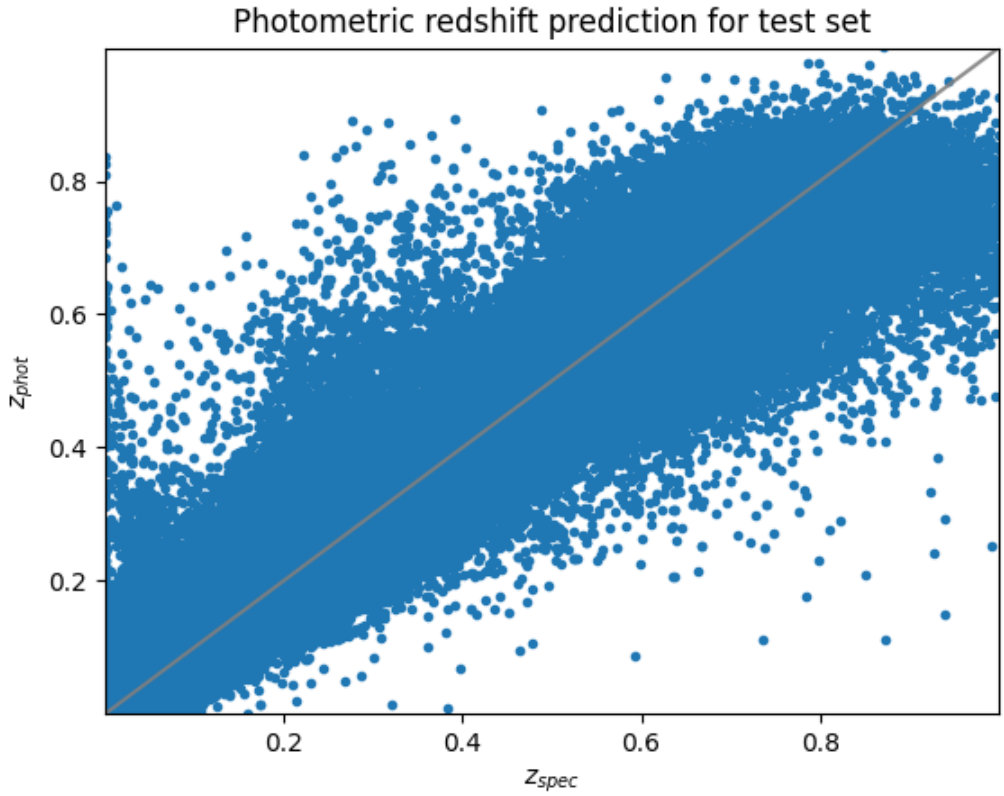

Figure 3.2: Predictions for test data

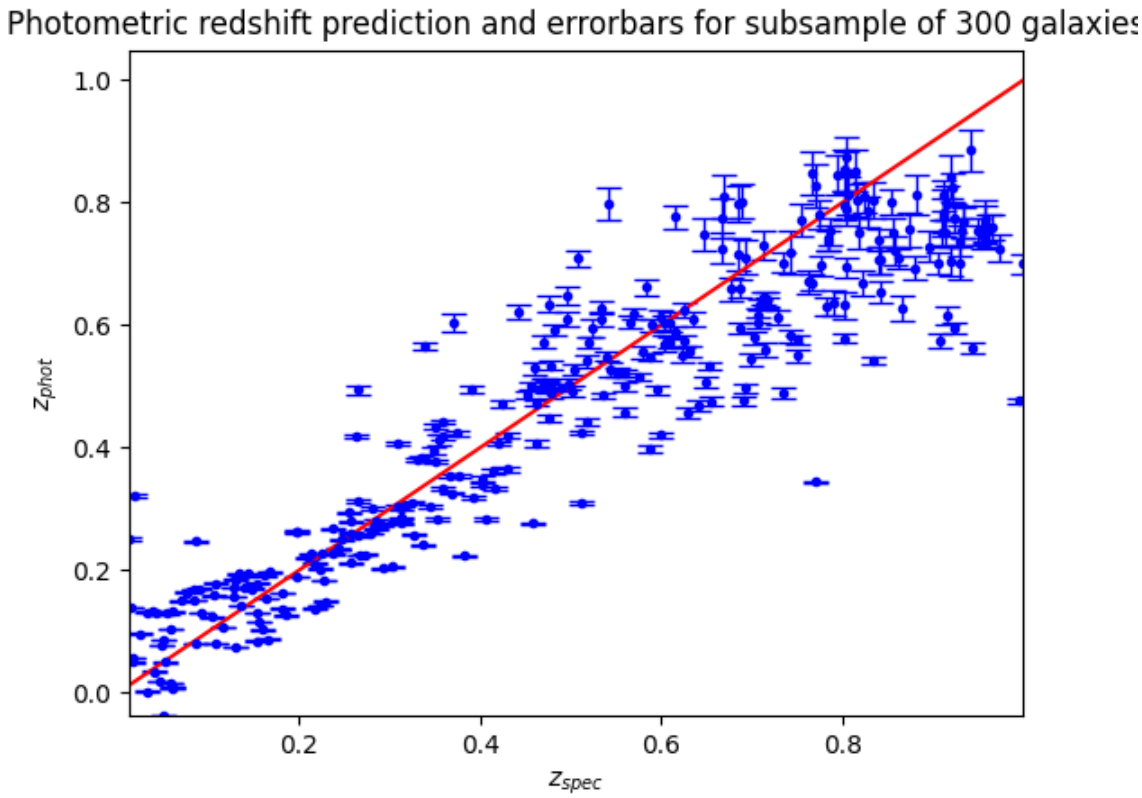

Figure 3.3: Photometric redshift prediction and errorbars for a representative subsample of 300 galaxies. The errorbars are due to errors in the photometric data and so depend on the particular model chosen for z_{phot}

References

[1] A. G. Riess, A. V. Filippenko, P. Challis, A. Clocchiatti, A. Diercks, P. M. Garnavich, R. L. Gilliland, C. J. Hogan, S. Jha, R. P. Kirshner et al. Observational evidence from supernovae for an accelerating universe and a cosmological constant. *The Astronomical Journal* 116, (1998) 1009.

[2] S. Perlmutter, G. Aldering, G. Goldhaber, R. Knop, P. Nugent, P. G. Castro, S. Deustua, S. Fabbro, A. Goobar, D. E. Groom et al. Measurements of Ω and Λ from 42 high-redshift supernovae. *The Astrophysical Journal* 517, (1999) 565.

[3] B. E. Schaefer. The Hubble diagram to redshift$>$ 6 from 69 gamma-ray bursts. *The Astrophysical Journal* 660, (2007) 16.

[4] L.-X. Li. Variation of the Amati relation with cosmological redshift: a selection effect or an evolution effect? *Monthly Notices of the Royal Astronomical Society: Letters* 379, (2007) L55–L59.

[5] S. Basilakos and L. Perivolaropoulos. Testing gamma-ray bursts as standard candles. *Monthly Notices of the Royal Astronomical Society* 391, (2008) 411–419.

[6] F.-Y. Wang, S. Qi, and Z.-G. Dai. The updated luminosity correlations of gamma-ray bursts and cosmological implications. *Monthly Notices of the Royal Astronomical Society* 415, (2011) 3423–3433.

[7] L. Tang, X. Li, H.-N. Lin, and L. Liu. Model-independently calibrating the luminosity correlations of gamma-ray bursts using deep learning. *The Astrophysical Journal* 907, (2021) 121.

[8] D. M. Scolnic, D. Jones, A. Rest, Y. Pan, R. Chornock, R. Foley, M. Huber, R. Kessler, G. Narayan, A. Riess et al. The complete light-curve sample of spectroscopically confirmed SNe Ia from Pan-STARRS1 and cosmological constraints from the combined pantheon sample. *The Astrophysical Journal* 859, (2018) 101.

[9] N. Suzuki, D. Rubin, C. Lidman, G. Aldering, R. Amanullah, K. Barbary, L. Barrientos, J. Botyanszki, M. Brodwin, N. Connolly et al. The Hubble Space Telescope cluster supernova survey. V. Improving the dark-energy constraints above z$>$ 1 and building an early-type-hosted supernova sample. *The Astrophysical Journal* 746, (2012) 85.

[10] C. E. Rasmussen. Gaussian processes in machine learning. In Summer school on machine learning. Springer, 2003 63–71.

[11] C. Escamilla-Rivera, M. A. C. Quintero, and S. Capozziello. A deep learning approach to cosmological dark energy models. *Journal of Cosmology and Astroparticle Physics* 2020, (2020) 008.

[12] N. Srivastava, G. Hinton, A. Krizhevsky, I. Sutskever, and R. Salakhutdinov. Dropout: a simple way to prevent neural networks from overfitting. *The journal of machine learning research* 15, (2014) 1929–1958.

[13] Y. Gal and Z. Ghahramani. A theoretically grounded application of dropout in recurrent neural networks. *Advances in neural information processing systems* 29.

[14] F. Pedregosa, G. Varoquaux, A. Gramfort, V. Michel, B. Thirion, O. Grisel, M. Blondel, P. Prettenhofer, R. Weiss, V. Dubourg, J. Vanderplas, A. Passos, D. Cournapeau, M. Brucher, M. Perrot, and E. Duchesnay. Scikit-learn: Machine Learning in Python. *Journal of Machine Learning Research* 12, (2011) 2825–2830.

[15] G. D'Agostini. Fits, and especially linear fits, with errors on both axes, extra variance of the data points and other complications. *arXiv preprint physics/0511182* .

[16] D. Foreman-Mackey, D. W. Hogg, D. Lang, and J. Goodman. emcee: The MCMC Hammer. *PASP* 125, (2013) 306–312.

[17] M. Abadi, A. Agarwal, P. Barham, E. Brevdo, Z. Chen, C. Citro, G. S. Corrado, A. Davis, J. Dean, M. Devin, S. Ghemawat, I. Goodfellow, A. Harp, G. Irving, M. Isard, Y. Jia, R. Jozefowicz, L. Kaiser, M. Kudlur, J. Levenberg, D. Mané, R. Monga, S. Moore, D. Murray, C. Olah, M. Schuster, J. Shlens, B. Steiner, I. Sutskever, K. Talwar, P. Tucker, V. Vanhoucke, V. Vasudevan, F. Viégas, O. Vinyals, P. Warden, M. Wattenberg, M. Wicke, Y. Yu, and X. Zheng. TensorFlow: Large-Scale Machine Learning on Heterogeneous Systems 2015. Software available from tensorflow.org.

[18] D. P. Kingma and J. Ba. Adam: A method for stochastic optimization. *arXiv preprint arXiv:1412.6980* .